LBL-24074

Lawrence Berkeley Laboratory
UNIVERSITY OF CALIFORNIA

Materials & Chemical Sciences Division

Microstructure and Magnetic Properties of Cobalt-Chromium Alloys

L.H. Chan
(M.S. Thesis)

September 1987

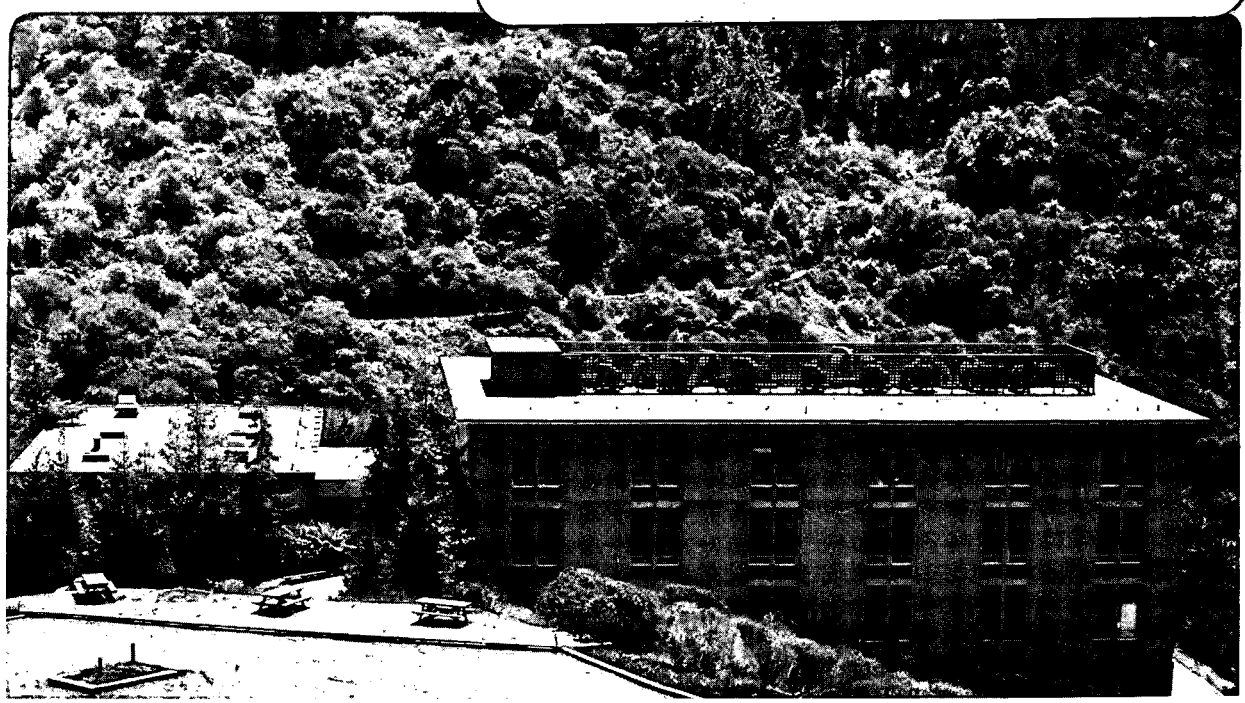

Prepared for the U.S. Department of Energy under Contract DE-AC03-76SF00098

LBL-24074

DISCLAIMER

MICROSTRUCTURE AND MAGNETIC PROPERTIES OF COBALT-CHROMIUM ALLOYS

L.H.Chan
[M.S. Thesis]

Department of Materials Science and Mineral Engineering
Materials and Molecular Research Division
Lawrence Berkeley Laboratory
University of California, Berkeley
Berkeley, CA 94720

This research was supported by the Director, Office of Energy Research, Office of Basic Energy Sciences, Materials Sciences Division of the U.S. Department of Energy under Contract No. DE-AC03-76SF00098.

CONTENTS

1. Introduction

1.1 General

Thin film magnetic recording media have evolved to meet the high storage densities needed for today's miniature devices.The use of continuous ferromagnetic thin films instead of conventional particulate media promises to increase data storage by more than one order of magnitude [White,1980].

The advantages of thin film media are: high packing density of magnetic material, the use of high saturation magnetization materials, and good uniformity at very low thicknesses. Conventional particulate media consists of oxide particles such as γ-Fe_2O_3 or CrO_2 which are randomly dispersed in a polymer matrix. The packing density of magnetic particles is 3-4 times lower in comparison to the continuous metallic films whose packing density of magnetic material can be as high as unity. Higher saturation materials such as cobalt and cobalt-based alloys are used in thin film media which results in sufficiently high recorded signals even at very low thicknesses. Moreover, high density recording systems require that the media be thin, defect free and of good uniformity which are readily achievable by sputtering and evaporation techniques of thin film preparation.

Two modes of recording are available to thin film media, longitudinal and perpendicular. In longitudinal recording, the magnetization of each bit is in the plane of the film, while in perpendicular recording the magnetization is normal to the film plane. Of the two modes of recording, the perpendicular mode is more suited for achieving ultra-high recording recording densities[Iwasaki and Nakamura,1977; Iwasaki, 1978].

Pure cobalt in its hexagonal form has high uniaxial

magnetocrystalline anisotropy and high saturation magnetization. Both of these properties are desirable for thin film recording media. However, the requirements for perpendicular recording is that the anisotropy field, $2K/M_S$ be greater than the maximum demagnetizing field, $4\pi M_S$ (where K is the magnetocrystalline anisotropy constant for the material and M_S is the saturation magnetization) Pure cobalt, however, does not fulfill the requirement for perpendicular anisotropy because its saturation magnetization is high in comparison to its magnetocrystalline anisotropy. Small additions of Cr have been found to decrease the saturation magnetization of the Co [Farcas, 1937] sufficiently to attain perpendicular anisotropy. This has been found to be achieved for alloys Cr concentrations of 14 at.%-22 at.% Cr. [Iwasaki and Ouchi, 1978].

Iwasaki, Ouchi and Honda [1980] have investigated the additions of Mo, W, V, Ti, and Mn to Co and evaluated the perpendicular anisotropy of the resultant films. Although Mo, W and V also exhibit perpendicular anisotropy, the resultant films had much lower coercivities in comparison to CoCr thin films. To date, cobalt-chromium is considered to have intrinsically superior properties and is the system of choice for ultra-high density thin film recording media [Ouchi and Iwasaki, 1987].

1.2 The Cobalt-Chromium System

The Co-Cr phase diagram has been investigated by several researchers [Allibert et.al.,1978, Elsea et.al.,1949, Grigor'ev et.al.,1961, Hansen,1958,, and Metcalfe,1953]. Figures 1 and 2 are the phase diagrams reported for the Co-Cr system by Hansen and Grigor'ev et.al. The region of interest for thin film applications lies between the

compositions of 14-22 at.% Cr. The interest in thin films has motivated extensive studies in this system in the narrow region of the phase diagram [for instance, see the review by Howard, 1986]. Studies of the Co-Cr system outside the interest of thin films have been confined to the measurement of magnetic properties. Bolzoni et.al.[1983] have studied the influence of Cr content on the Curie temperature, saturation magnetization, and anisotropy field. These were all found to decrease with Cr content. The alloys are found to be non-magnetic for Cr contents in excess of 27 at.% Cr.

Referring to the low Cr region (<20 at.% Cr), of the phase diagram (Figures 1 and 2), pure Co and the alloys exhibit a high temperature face-centered cubic phase(fcc) and a low temperature hexagonal close-packed phase (hcp). In pure Co, the allotropic transformation is found to be martensitic in nature [Nishiyama, 1978]. As can be seen from figures 1 and 2, the low temperature (<700^{o}C) phase equilibria in the cobalt -rich region have not been firmly established, presumably due to slow diffusion. Grigor'ev et.al. have reported on the existence of a series of intermediate phases related to the ε-Co (hcp-phase). Recently, Bolzoni et.al. [1978] have attempted to determine the hcp<-->fcc and the transformation temperatures on heating and cooling. They observed a hysteresis, characteristic of martensitic type transformations, which increases with Cr content. As these authors have asserted, this region of the phase diagram remains uncertain and further investigations need to be carried out.

While the microstructural details and magnetic properties of Co-Cr in the thin film form are being extensively investigated, the same is not the case for the bulk Co-Cr alloys. Thus, it is worthwhile to consider Co-Cr as a metallurgical system, rather than an economically viable

magnetic recording medium. A systematic study would provide information on various aspects of the system such as phase equilibria, microstructure, magnetic, mechanical, and physical properties. Variables to consider are composition, thermal history, and ternary additions.

This particular study will attempt to address a few of these points. Specifically, the objectives of this study are to investigate:

-the microstructural evolution of these alloys as function of Cr content,

-the magnetic properties of these alloys as function of Cr content and

-to extend this understanding to elucidate the microstructure/ property correlations.

2. Experimental Procedures

2.1 Material Fabrication

Cobalt chromium alloys of five chromium compositions were fabricated by the Materials Research Corporation, Orangeburg, NY, by vacuum melting. The compositions under study are 1.44, 5.0, 10.0, 15.2 and 20.0 atomic % Cr. These compositions were chosen because they encompassed two extremes, that of pure cobalt and that used for Co-Cr thin film applications (14-22 at% Cr). The samples were obtained as as-cast cylinders that were 1 cm in diameter and 1 cm long.

2.2 Homogenization Treatments

As cast samples of the five different chromium compositions were encapsulated in quartz tubes backfilled with helium and homogenized for 70 hours at 1100° C. The samples were then water quenched. These samples will henceforth be referred to as H1 samples.

2.3 Grain Refining Treatment

In order to investigate the effect of grain size on the magnetic properties, grain size refining treatments were done. This consisted of deforming the samples from a thickness of 1 cm to 1 mm by hot rolling at 900° C with four passes. The motivation behind this was to introduce nucleation sites. Cracking, especially for the higher Cr samples required an intermediate reheat of 1 minute at 900° C between the first and second passes.

The hot rolled samples were subsequently hot rolled at 870° and 770° C, respectively for 15 minutes and then water quenched. These are referred to as H2 and H3 samples

respectively.

2.4 Equilibrium Annealing Treatment

As cast samples of 10.0 and 15.0 at% Cr were homogenized at 1000° C for 50 hours, quenched and then aged at 620° C for 700 hours. The samples were enscapulated in quartz and back filled with helium prior to any heat treatment. This annealing treatment was done in order to obtain equilibrium microstructures and to compare these to the microstructures observed in the as-quenched samples (H1). These two compositions were chosen since they appear to lie well within the single phase field in the Co rich region of the Co-Cr phase diagram (Figure 1).

2.5 Phase Analyses

The phase content of the bulk alloys was characterized by x-ray diffraction in a Siemens Diffractometer using Cu K_α radiation at a scan rate of 0.9°/min. Initially mechanically polished surfaces were used to characterize the phases present. However preliminary tests showed that mechanical polishing could lead to phase transformations at the surface. Hence samples were thereafter electropolished after mechanical polishing to remove any surface transformation products.

Quantitative estimate of the amount of hcp phase in the alloys was obtained from equation (1) derived by Stage and Guillard [1950] for the calculation of weight % of hcp phase in pure cobalt.

$$\text{wt\% hcp} = \frac{I_{(10\,\bar{1}1)\text{hcp}}}{I_{(10\,\bar{1}1)\text{hcp}} + 1.5\, I_{(200)\text{fcc}}} \times 100 \quad (1)$$

where I is the integrated intensity of the indicated peak.

Equation (1) takes into consideration both the structural and multiplicity factors. The calculated weight percent of the hcp phase for the alloys is an estimate and not an accurate quantitative measurement because equation 1, which has been derived for a polycrystalline powder sample, is not adequately corrected for grain size effects.

2.6 Magnetic Measurements

Magnetic hysteresis loops were measured using a Princeton Applied Research vibrating sample magnetometer (VSM) at a frequency of 80 Hz. Samples for magnetic measurements were in the form of disks of 3 mm diameter, 75 - 100 μm in thickness. The hysteresis loops were measured in the plane of the sample. The measured properties were saturation magnetization, M_s and intrinsic coercivity, iHc.

2.7 Microstructural Characterization

2.7.1 Light Optical Microscopy

Specimens were mechanically ground using Si-C papers of 240,320,400 and 600 grit. The ground surfaces were subsequently electropolished using a solution of 640 ml of ethyl alcohol,140 ml of butoxyl alcohol and 220 ml of perchloric acid. Electropolishing conditions of 50 - 55 Volts were used. The samples were then etched in a solution of 60 ml HCl, 15 ml HNO_3, 15 ml CH_3COOH and 15 ml H_2O.

The etched specimens were examined with a Zeiss Axiomat optical microscope. Grain size measurements were performed using the intercept method and the calculated grain size for each sample is an average of ten intercepts.

2.7.2 Transmission Electron Microscopy

Specimens for transmission electron microscopy were prepared from bulk samples using the following procedure. Slices of approximately 0.4 μm in thickness were cut using a Buehler diamond saw lubricated with kerosene. The slices were mechanically ground with successively finer grit SiC paper until the specimen thickness was 150 μm. Samples of 3 mm diameter were mechanically punched from the ground specimens and further thinned to 100 μm by lightly grinding with alumina paper.

Since low chromium samples are strongly magnetic it was necessary to minimize the volume of the specimen in order to minimize the associated magnetic effects in the electron microscope. This was achieved by using 2.3 mm samples.

The samples were then made electron transparent by electropolishing using the electrolyte described above. Voltages used increased proportionally with the Cr content and ranged from 15 V for the low Cr compositions to 30 V for the highest Cr samples.

Conventional electron microscopy techniques of bright field and dark field imaging and diffraction were used to characterize the microstructure. The samples were examined in the Philips 301 and Philips 400 Electron microscopes operated at 100 kV.

Chemical analysis was done using the technique of energy dispersive x-ray spectroscopy (EDXS) on the Philips 400 microscope using a nominal probe size of 40 nm.

2.8 Observation of Magnetic Domains

2.8.1 Bitter Powder Method

In order to observe the magnetic domains and domain wall motion the surface of samples, 150 μm in thickness, were electropolished. The electropolishing was done using the electrolyte described in section 2.6 and was carried out to produce a stress free surface. A drop of colloidal suspension containing ferromagnetic particles of Co, 100 Å in diameter was placed on the polished surface and covered with a thin cover glass to spread the suspension evenly. The specimens were examined with a Zeiss Axiomat optical microscope. An external magnetic field of up to 1.5 kG was applied using a Sm-Co permanent magnet in order to observe domain wall motion. The normal and in-plane field components were varied by varying the distance between the magnet and the sample vertically and horizontally, respectively. The field values at the sample were measured using a Bell Hall probe and a Bell digital gaussmeter.

2.8.2 Transmission Lorentz Microscopy

The observation of magnetic domains and domain walls at high resolution and their interaction with microstructural features was possible in the electron microscope for thin samples, using Lorentz Microscopy.

The path of electrons passing through a specimen will be deviated, by an amount and in a direction determined by the local magnetization vector. For a uniaxial material with 180° domain walls and with its magnetization in the plane of the sample, the path of the electrons is shown in figure 3. Electrons are deviated in opposite directions in adjacent 180° domains leading to a deficiency of electrons in A and excess

at B. In order to observe domain walls, the objective lens is focussed above or below the sample and hence the width of the domain boundary depends on the amount of defocussing.

The Philips 400 Electron microscope was used to image magnetic domains. In order to avoid saturation of the samples, it was necesary to operate the microscope in the low magnification (LM) mode. In this mode, the objective lens is fed with low fixed currents so that the image crossover occurs at the plane of the diffraction aperture. This mode however limits the maximum magnification to 2200X.

The weak in-plane component of the objective lens field was used to move the domain walls. Upon tilting, the in-plane component changes. Hence, observations of domain wall motion and its interaction with microstructural features were possible. Unfortunately, quantification of fields at the sample was not possible.

3.EXPERIMENTAL RESULTS

3.1 Phase analysis

Figure 4 (a-e) is a set of x-ray spectra collected from homogenized and quenched samples (H1) of the five chromium compositions under study. The (200) fcc peak was used to monitor the presence of the fcc phase since it is the only fcc peak which does not lie near a hcp peak as can be observed in the standard (Figure 4f). The high temperature fcc phase is stabilized and retained at room temperature for samples of compositions including and greater than 5 at% Cr. To the detectibility of x-ray diffraction, no fcc phase was found in the samples of 1.44 at% Cr.

The set of x-ray spectra collected from samples which were deformed and recrystallized at 870^{o}C for 15 minutes (H2) are shown in figure 5. Evaluation of the relative intensities of the (200) fcc and (10 $\bar{1}$1) hcp peak shows a systematic increase in the amount of fcc phase retained (Fig.6). The decrease in the fcc phase content observed for the 15.2 at% Cr can be attributed to the line broadening observed for the (10 $\bar{1}$1) hcp peak which leads to a smaller ratio. Figure 6 is meant to provide an estimate rather than the absolute values of retained fcc phase as a function of chromium.

Figure 7 is the set of x-ray spectra collected for the equilibrium (H4) samples. It can be seen that only the hcp phase is present at equilibrium and that no fcc phase is retained. Moreover, to the detectibility limit of XRD, no other phases were observed.

3.2 Magnetic Properties

Figures 8 a,b, and c are plots of saturation magnetization as a function of Cr content for H1, H2, and H3 samples, respectively. The saturation magnetization of all the specimens decreases linearly with Cr content which is in agreement with previously reported data [Bolzoni et.al.,1983].

The intrinsic coercivity of the H1 samples is plotted as a function of Cr composition in Figure 9. The intrinsic coercivity is observed to be low in these samples and nearly invariant (~30 Oe) with Cr content.

The intrinsic coercivity as a function of grain size was investigated for all the alloys H1, H2 and H3. For each Cr composition, three grain sizes over a range of 500 μm to 20 μm were studied. Figure 10 is a plot of the intrinsic coercivity as a function of log average grain size for compositions of 1.44 at% Cr and 20 at% Cr. In all compositions, a small increase in coercivity was observed with decreasing grain size; however, absolute values of the coercivity remain fairly low (< 50 Oe). The increase in coercivity with decreasing grain size was most prominent for samples of 1.44 at% Cr. The increase in coercivity as a function of grain size was less pronounced with increasing Cr content.

The intrinsic coercivity of the equilibrium annealed H4 samples of composition 10 and 15 at% Cr. sample were measured to be 30 $\pm$ 5 Oe and 15 $\pm$ 5 Oe, respectively.

3.3 Microstructural Characterization

3.3.1 Optical Microscopy

Figure 11 (a-e) shows the observed etched microstructures of the H1 samples for compositions of 1.44, 5.0, 10.0, 15.2, and 20.0 at% Cr, respectively. The average grain size of the samples was found to range between 500-600 μm. As can be seen in Figure 10 a-e, the microstructure suggests that the fault density increases with Cr content in the alloys . Quantification of the relative amounts of fcc and hcp phases from the etched microstructures was difficult due to the fact that both phases were found within a single grain, as explained in the following section. Furthermore, both phases found within a grain were faulted.

The optical microstructure of samples H2 and H3 for the five Cr compositions are shown in Figures 12 and 13 (a-e) respectively. .In the H2 samples the microstructure indicates that the faulting increases with increasing Cr content. H3 samples also exhibited the same behavior except for the highest (20 at%) Cr sample. This anomaly may be explained by the fact that at 770^{o}C, from which temperature the 20 at% Cr sample was annealed and quenched, only the hcp phase is stable. (Fig. 1).

The average grain size of the samples H2 and H3 was found to vary with Cr content. Figure 14 is plot of the grain size as function of Cr content for H2 samples. The average grain size for both the heat treatments H2 and H3 was observed to decrease with Cr content; however, the trend is more pronounced for H2 samples.

Figures 15a and 15b are light optical micrographs of H4

samples of 10 at% Cr and 15 at% Cr, respectively. Comparing these micrographs with figures 11 c-d, it can be seen that the stacking fault density has decreased considerably.

3.3.2 Transmission Electron Microscopy.

Homogenized and Quenched (H1)

Figure 16 is a bright field electron micrograph of a H1 sample of 15 at% Cr composition. It is representative of the general microstructure of H1 samples of Cr content of 5 at% or greater. In alloys (5 - 20 at% Cr) with this treatment, two phases are present. Within a single grain, the hcp phase appears as bands of highly faulted material embedded in the fcc phase. The amount of fcc phase appears to increase with Cr content.

The faults in the hcp phase are observed to lie on (0001) basal planes, these being the close packed planes in the hcp lattice. This is shown in figure 17 which is a bright field/ dark field image pair of the faults, on edge, in the hcp phase. The faults were imaged in dark field using a streak along the [0001] direction.

The faults in the fcc phase are observed to lie on all four {111} planes. This is shown in figure 18, a bright field image from a fcc region in a [101] zone axis. Stacking faults tend to occur along close packed planes and are therefore easily explained as the {111} planes are the close packed planes in fcc. This faulting could manifest itself as streaks in the diffraction pattern. However depending on the orientation of these streaks to the Ewald sphere (which is

dependent on the fault orientation) ther streaks may appear as streaked lines or spots (figure 19). Analysis of such spots or streaks would enable the characterization of these faults to be done. It must however be kept in mind that extra spots could arise due to other effects such as double diffraction ordering or twinning. By diffraction analyses, it is posssible to unequivaocally determine the origin of such extra spots. In figure 18 taken on a [101] zone axis, the 11 $\bar{1}$, and the $\bar{1}$11 faults are viewed on edge (marked 1 & 2 respectively). The other two variants of the {111} faults (1 $\bar{1}$1 and 111, labeled 3 & 4) are inclined at 35° to the foil normal and show fringe contrast, as can be seen in the figure. These two fault variants are responsible for the two extra spots observed about each diffracted spot in the diffraction pattern.

To determine the nature of the stacking faults, bright field/dark field (BF/DF) imaging of the faults was carried out. Figure 20 shows one such BF/DF image in a [001] zone axis. The bright field was imaged using the 020 reflection and the centred dark field was imaged using the 0 $\bar{2}$0 reflection. All four {111} variants of the faults lie inclined to the foil surface with an angle of 55° and they are responsible for the four satellite spots observed about each diffracted spots. The top and bottom of the fault are labelled T and B respectively. It can be seen that fringe contrast reversal occurs at the top of the foil in Figure 20. Using the method of Hashimoto *et.al.* (1962) the faults were therefore determined to be intrinsic.

The observed orientation relation between the fcc and hcp phases for the alloys over the composition range of (5 at% - 20 at% Cr) is :

$$(0001)_{hcp} // (111)_{fcc}$$
$$[11\bar{2}0]_{hcp} // [1\bar{1}0]_{fcc}$$

The relation is known as the Shoji-Nishiyama relationship (S-N relation) and it is the same as that observed for pure Co. It indicates that the close packed planes of the two phases are parallel. Figure 21 is a bright field micrograph taken on a fcc $[1\bar{1}0]$ zone axis. It can be seen that there are two hcp variants, on a $[11\bar{2}0]$ zone, as shown in the diffraction patterns 21 a and d, alongside the fcc phase. The diffraction pattern 21c is from the interface between the fcc and one of the hcp phase variants. This figure illustrates the orientation relationship shown in the above expression.

In H1 samples of 1.44 at% Cr, no fcc phase was detected. In the absence of the fcc phase, the regions of hcp no longer appear as bands; however within a grain, several regions of hcp phase with definite crystallographic relationships are observed (figure 22). It can be seen that two regions of hcp phase share a common $[1\bar{2}10]$ zone, as shown in the diffraction patterns from each region (22 a and c) and the faults in both regions are edge on. The interface between the two regions is faceted (arrowed). The facets of the interface coincide with the $[10\bar{1}0]$ directions of each hcp region.

Figure 23 is a BF/DF image of the faults viewed on edge in a $[1\bar{2}10]$ zone. The dark field image which was formed using a [0001] streak clearly shows that faulting occurs on the basal (0001) plane. Attempts were made to determine the nature (intrinsic or extrinsic) nature of the faults by observing the contrast in the outer fringes when the faults are imaged with reflections (hkil) such that $h - k = -1$

[Hitzenberger,1985]. The difference in contrast observed when l is even and when l is odd determines the nature of the fault. However, the fault density was such that the fringes from the faults overlapped and analysis was not possible as shown in figure 24 in which the faults were imaged using $\mathbf{g} = 01\,\bar{1}\,\bar{1}$ on a $[1\,\bar{2}13]$ zone.

Equilibrium (H4)

In both the 10 and 15 at% Cr sample, only hcp phase was detected. The aging treatment led to a considerable decrease in the fault density; however, it did not remove all the faults within the hcp phase (Figure 25). The faults have been imaged on a $[1\,\bar{2}10]$ foil orientation and therefore are observed on edge.

3.3.3 Energy Dispersive X-ray Spectroscopy

In H1 samples the composition of the fcc and hcp phases were found to be uniform for compositions of 5 at% Cr and higher. This is in agreeement with the nature of the transformation which maintains that parent and transformed phases are of the same composition.

In H4 samples of Co-15 at% Cr, no second phases were observed. Chromium segregation to the grain boundaries was investigated; however no segregation was detected. Table 1 shows a typical analysis from grain interiors and from grain boundaries. (The Cr content given by the EDXS analysis is higher than that quoted as the Cr content of the bulk alloys. Flourescence of Cr (Z=24) by Co (Z=27) may account for

the higher Cr content found by the thin film analysis which does not take into account flourescence. Moreover, flourescence of Cr from the microscope column can also lead to higher Cr counts. However, EDXS was used to compare the relative Cr content from different regions within a sample and not to establish the absolute Cr content.

The grain size of H2 and H3 samples which were deformed and recrystallized at 870^0C and 770^0C for 15 minutes, respectively decreased with Cr content. Since Cr segregation to the grain boundaries can influence the recrystallization and grain growth behavior, the role of Cr segregation was investigated in samples of 5 at% Cr and 20 at% Cr. Typical analysis of spectra was collected from grain interiors and grain boundaries Table 2 tabulates the chemical analysis from these regions . It can be seen that the Cr content does not differ by more than 1% suggesting that the Cr distribution is uniform.

3.4. OBSERVATION OF MAGNETIC DOMAINS AND DOMAIN WALL INTERACTIONS WITH MICROSTRUCTURAL FEATURES

3.4.1 Bitter Powder Method.

Figure 26 is an optical micrograph showing the magnetic domain pattern observed on the basal plane (i.e., c-axis normal to the surface) of H1 (1.44 at% Cr) under an applied normal field of ~ 1kOe. The externally applied field polarizes the colloid particles so that they collect at the surface of domains where the applied vector and the magnetization vector are parallel. Hence the dark regions of the pattern are interpreted as regions of magnetization which are parallel to the field while the light regions correspond to domains with their magnetization opposite to the applied field.

The observed structure consists of a wavy pattern of oppositely magnetized regions. Near the surface, spike domains have formed and they are arranged in a hexagonal pattern. Wavy and spike domains are shown schematically in figures 27 a and b, respectively. The curved walls and the surface spike domains result in a decrease of magnetostatic energy due to a greater mixture of opposite poles at the surface [Chikazumi,1964]. Curved walls will increase domain wall energy and are observed in thin samples only. Spike domains also increase wall energy but not considerably because they are short.

The same patterns were observed in samples up to 15 at% Cr, (Figure 28 b) although the magnetostatic energy should be considerably lowered due to the lower saturation magnetization in the higher Cr samples. The left grain in Figure 28a shows the case when the magnetization is in the plane of the sample surface. The colloid particles are attracted to the regions of highest field gradient, this being at the domain walls. The pattern consists of parallel bands of colloid separated by regions of opposite magnetization. Near the grain boundaries, the width of the domains become increasingly smaller and this can be attributed to the formation of spike domains in order to decrease the free pole density. This is shown in Figure 29.

Domain walls between domains with their magnetization in the plane of the sample were observed to move readily under the application of very low fields (~1 kOe) parallel to the sample surface. This indicates high virgin permeability.

The interpretation of magnetic domain structures observed from the surface of samples is relatively straight forward for

single crystals in which the surface can be made parallel or normal to the easy axis of magnetization . Interpretation becomes considerably difficult for polycrystals where the surface of individual grains make random angles with the easy axis of magnetization, resulting in complex patterns. Moreover, the interpretation of Bitter patterns from highly faulted quenched samples was difficult as shown in the case of figure 30. The ferromagnetic particles were observed to decorate the intersection of faults with the surface . This can be explained by interpreting the faults as microscopic grooves, in the otherwise flat electropolished surface. At the site of the grooves, free poles develop and a field gradient exists to attract colloid particles. This observation in conjunction with the low resolution of the technique does not provide information concerning the interaction of the domain walls and the faults. Hence higher resolution techniques such as Lorentz microscopy were used to image magnetic domains, domain walls and to establish their interaction with faults and grain boundaries.

3.4.2 Lorentz Microscopy

Both the fcc and hcp phases are ferromagnetic. The easy axis of magnetization for the hcp phase is the [0001] direction and for the fcc phase, the four <111> directions.

In the hcp phase, the magnetocrystalline anisotropy is high and the magnetization lies along the easy axis of magnetization, the c-axis, except at high temperatures [Watanabe,1985]. As observed in TEM, the faults in the hcp phase lie on (0001) planes and hence, the domain walls will intersect the faults in the hcp phase at 90^{o}. This can be seen in Figure 31 which is a Lorentz micrograph from a H1 sample of

5 at% Cr. The orientation of the foil in figure 31 is [2 $\bar{4}$23] corresponding to the C-axis being tilted 35^{o} from the plane of the sample. Domains of opposite magnetization are labelled on the figure. The stripe domains observed in these alloys are similar to those observed for pure Co.

The width of the domains are dictated by the angle between the easy axis and the specimen surface. For magnetization in the plane of the sample, the width of the domains is large and as the magnetization component tilts away from the plane of the sample, more surface poles are formed and the magnetostatic energy is decreased if more domains are formed . Hence, the domain width decreases. (The difference in the width of the domains is due to the field of the objective lens being oriented favourably with respect to one set of domains and unfavourably with respect to the other [Silcox,1963]).

Figure 32 shows the magnetic domain pattern from a region populated with thin bands of fcc and hcp phases in a H3 sample of 5 at% Cr. Again the domain walls in the hcp phase are parallel to the [0001] direction and in this micrograph, the regions of hcp are identified as those consisting of parallel lines running normal to the interface between the two phases. As mentioned above, since the domains are of unequal widths, the c-axis of the hexagonal phase must not be in plane. The impression may be obtained that within a given phase, the domain pattern is simply that of a single crystal, but this is an over simplification; in fact the structure is modified by the interaction between the two phases which takes the form of continuity in the domain wall across the interface of the two phases. This does not completely avoid formation of free poles, but does reduce the effect. Hence in the fcc

phase, the walls take a configuration which tends to maintain continuity of the magnetization across the two phases.

The 180^{o} Bloch walls observed in the thick regions (>700å) shown in Figure 31 has magnetization vectors which rotate about the axis normal to the wall and free poles are formed where the wall intersects the surface of the sample. However, as the film thickness decreases, the magnetostatic energy created by the free poles can be appreciable. In order to decrease the magnetostatic energy, the magnetization vector rotates not about the wall normal but about an axis normal to the film plane. Such walls are termed Neel walls. At the transition region between the two domain wall structures, cross tie wall are observed to have lower domain wall energies. A cross tie wall consists of alternating Neel segments separated by segments of Bloch lines. Discontinuities of this type allow a domain wall to be subdivided into segments of alternate magnetic moment. Figure 33 shows such cross-tie walls near the edge of the sample

Figure 34a from a H3 sample of 5 at% Cr shows a domain wall intersecting bands of the fcc and hcp phases at a position between position 1 and 2. The domain wall is continuous across the interface of the two phases. At the interface, free poles are likely to form if the magnetization of the two phase are not coincident. In the hcp phase, the domain wall is very straight and undeviated from the [0001] easy axis. Figure 34b shows the domain wall at position 2 after tilting of the sample. Below the arrows, the wall has moved smoothly in the hcp phase, unrestricted by the faults which run normal to the wall. The wall, however, drags behind in the fcc regions. The fcc regions are easily recognized as those regions which show several variants of the {111} fault

planes. Domain wall interaction with the faults in the fcc region was observed to vary depending on the angle between the faults and the domain wall. When the domain wall intersects the fault at 90^{o}, no interaction was observed and when the domain wall is parallel to the faults, weak pinning was observed.

This can be explained as follows. Assume that the wall energy is a function of the wall position and that the energy of the wall is lowered near the stacking fault. Displacement of the wall that is normal to the stacking fault will not change the energy of the wall as compared to the original position. Hence, the wall moves easily into the new position to minimize the overall magnetic energy corresponding to that particular value of the in-plane component of the magnetic field of the objective lens. However, when the wall is parallel to the stacking fault, as it can be in the case of the fcc phase, then displacement of the wall from its "pinned" position at the fault, into the unfaulted region can lead to an increase in the wall energy. This means that the wall will have a tendency to "stick" to the fault interface, as is qualitatively observed in Figure 34. The angular dependence of the interaction between the faults and the domain wall has also been observed in ferrites by [Lin et. al., 1984].

Figure 35a shows a portion of the domain wall pinned at the fault at position 1. With a succession of two abrupt jumps, the wall has moved to position 2 (Figure 35b) and upon reversal of the field, the wall jumps back to position 1. This reversible wall movement inside the grains indicates, qualitatively, that the strength of pinning by the faults in the fcc phase is not very strong.

As discussed earlier, the domain walls in the hcp phase will always intersect the faults at 90° since the crystallography of the faults dictates that the faults lie on (0001) planes and the magnetocrystalline anisotropy dictates that the magnetization lie along the easy axis of magnetization, the [0001] direction. Hence, motion of domain walls in the hcp phase was observed to be unrestricted.

The domain wall in the fcc region is more flexible and need not necessarily run normal to the faults. Hence, weak interaction is possible. Moreover, the fcc phase which has four equivalent easy directions directions of magnetization has lower anisotropy. That the pinning of the domain wall by the fcc faults is not strong even when the faults lie parallel to the domain wall can be explained by the fact that both fcc and hcp phases are ferromagnetic. Hence, the exchange energy in the neighbourhood of the fault is not significantly different from that of the perfect crystal.

Figure 35a shows a domain wall intersecting a grain boundary at position 3 between grain 1 (G1) and grain 2 (G2). The wall intersects the grain boundary at near 90° . As for the case of stacking faults, the grain boundary interaction with the domain wall when the angle is close to 90^0 is very weak. This is shown in figure 35b where the domain wall has moved to position 4 by moving across the grain. The interaction of the grain boundary with domain walls is stronger when the domain wall and the grain boundary are parallel. Figure 36 shows a domain wall that has moved through grain 1 (G1) towards grain 2 (G2). Domain wall motion was observed to be effectively impeded at the grain boundary between G1 and G2. (The arrows indicate the region of the wall which runs parallel to the grain boundary.

4. DISCUSSION

X-ray diffraction and optical microscopy showed that the amount of fcc phase retained increased with increasing Cr content. Furthermore, optical microscopy and TEM observations showed that the extent of faulting increased with Cr content. The latter fact can be easily explained in light of the former since faulting in the fcc phase can occur on the four {111} planes, but can occur on only one plane, (0001) , in the hcp phase. The increase in fault density can be associated with a increase in the number of possible fault planes which can intersect the surface. Therefore, the contribution of the fcc phase to the fault density is much greater than that of the hcp phase.

In order to explain the phases present and the possible role of Cr content, it is necessary to examine the nature of the fcc-to-hcp transformation in Co and Co-based alloys. This fcc-to- hcp transformation has been established to be martensitic in nature.

Martensitic transformations are usually diffusionless, occur athermally and involve a shape deformation. The athermal nature of these transformations implies that they cannot occur isothermally, but can occur only by the lowering of temperature. These martensitic transformations do not start at a temperature T_o where the free energy of the parent and the daughter phases are equal ($\Delta F^{p->d} = 0$), but start only at a lower temperature, the martensite start temperature, M_s. The free energy change corresponding to the difference between T_o and M_s constitutes the driving force for the transformation. Further cooling below the M_s to an ambient

temperature, T_a adds an additional term to the driving force. As additives which decrease M_s, also and tend to decrease T_o [Nishiyama,1978], the term arising due to the undercooling from M_s to T_a tends to dominate the driving force. The extent of transformation is dependent upon undercooling; the larger the undercooling, the greater the driving force. Hence, as M_s temperature increases, the driving force, (M_s-T_a) increases.

Amongst the factors that affect the fcc-to-hcp transformation upon cooling are grain size and solute content as both of these parameters affect the transformation temperature. Additions to cobalt have been shown to influence the M_s temperature (for instance, decrease in the case of Ni). Therefore, it is reasonable to expect that the addition of Cr to Co would influence the transformation temperature.

Other researchers have shown that the addition of C and W monotonically increase the fcc phase content of Co-C and Co-W alloys [Roebuck et.al., 1984]. Mahajan and co-workers (1977) have similarly shown that Fe additions to Co tend to stabilize the fcc phase. C was found to be more effective in stabilizing the fcc phase and this was explained on the basis of expansions in the unit cell per atom additions. The expansion was much greater for C than it was for W. Such an expansion in the unit cell makes the fcc-to-hcp transformation energetically unfavorable and leads to the retention of the fcc phase.

To examine the effect of Cr additions on the lattice parameter of Co-Cr alloys, x-ray diffraction was carried out. However, within the resolution limits of x-ray diffraction the results proved to be inconclusive due to the low intensities at the high angles required for accurate lattice parameter

determinations and also due to the overlap of fcc and hcp peaks. Considering the atomic radii of Co and Cr (1.2530 å and 1.2490 å, respectively) additions of substitutional Cr to Co are unlikely to cause large changes in the unit cell dimensions. Hence changes in phase content cannot be attributed to changes in unit cell volume resulting from Cr additions.

The role of Cr then would appear to affect fcc phase retention through its influence on the M_S temperature. A lowering of the M_S temperature would retard the transformation since the driving force for transformation is reduced. It would appear that Cr additions to Co decrease the M_S temperature causing the retention of the high temperature fcc phase. This is substantiated by the work of Matsunaga and Wever and co-workers, who have determined the fcc->hcp transformation temperature on cooling [Elsea et. al., 1949]. They have found that beyond 5 at.% Cr, the tranformation temperature decreases with Cr content. In the range of 0-5 at.%Cr, there exists an inconsistency with the present work which may have to be investigated in greater detail.

Grain size measurements from optical microscopy revealed that the average grain size decreased with increasing Cr content (Fig.16). The ratio of the rate of nucleation, N to the rate of growth, G is frequently used to interpret recrystallization data. Assuming N and G are average values, for an isothermal recrystallization process, the recrystallized grain size can be related to this ratio.

When the N/G ratio is high, many nuclei will form prior to completion of the recrystallization process and a fine grain size will result. Another possible effect is the

retardation of grain growth rather than the enhancement of nucleation rate that contributes to grain size refinement. Since a retardation could result from solute segregation and subsequent impediment to grain boundary motion; however, EDXS spectroscopy did not reveal any solute segregation at the grain boundaries within the spatial resolution of the technique (200 Å). Therefore, given the same history for all the compositions and and the lack of solute segregation, it would appear that Cr increases the nucleation rate, leading to a finer grain size.

As grain boundaries serve to stabilize the parent phase and thus hinder the martensitic transformation, the observed decrease in grain size would lead to increased fcc phase retention. This is consistent with the x-ray diffraction and optical microscopy results discussed above. Thus, it would appear that Cr additions affect the M_s temperature both directly and indirectly through their influence on the grain size. The contribution of the latter effect is likely to be less significant than the former given the relatively large grain sizes (30-70μm) used in this study.

The saturation magnetization of the alloys was observed to decrease almost linearly with Cr content. This is consistent with the results reported in the literature [Bolzoni et.al., 1983]. Bolzoni and co-workers explain the decrease in saturation magnetization as caused by Cr atoms which carry a moment of 4.25 Bohr magnetons coupling antiferromagnetically with Co moments. Neutron diffraction data [Chen, 1986] supports the contention that the decrease in saturation magnetization is due to antiferromagnetic coupling of Co and Cr moments rather than by a dilution of Co moments by Cr.

The intrinsic coercivity for all the compositions studied was found to be low (~30 Oe.) and almost invariant with composition for a given heat treatment. The intrinsic coercivity, however, for a given composition showed a small increase with decreasing grain size. This effect decreased with increasing Cr content.

The coercivity is not an intrinsic property of the material, but is determined by the magnetization reversal mechanism [Livingston, 1981]. The reversal mechanism is strongly dependent on the microstructure (e.g., grain size, shape, stress) and impurities and defects such as voids and inclusions. There are two magnetization reversal mechanisms: rotation processes and domain wall processes. Rotation processes involve the reversal of magnetization direction continuously through coherent or incoherent rotation. On the other hand, domain wall processes are discontinuous and involve the nucleation and growth of domains of opposite magnetization. This growth occurs by the movement of the domain wall which is a region of transition in the magnetization direction between the two regions of opposite magnetization.

Crystalline and shape anisotropy are the prime impediments to magnetization reversal by rotation processes. Nevertheless, for sufficiently fine particles, the presence of a domain wall is energetically unfavorable and therefore the reversal mechanism must be confined to rotation processes.

In the present study, given the relatively large grain sizes, domain wall reversal mechanisms are most likely to be operative. Domain wall processes can be nucleation controlled

or growth controlled. Nucleation of reversed domains is most likely at surface irregularities with large demagnetizing fields and at defects where the crystal anisotropy is locally lowered. Growth of these reversed domains can be impeded by defects such as inclusions, faults and grain boundaries which pin the domain walls, altering the domain wall energy locally. Thus, domain wall processes are likely to be sensitive to microstructure.

The observed dependence of the intrinsic coercivity on the grain size is in agreement with the results obtained by other researchers for $SmCo_5$ [McCurrie and Carswell, 1970] and for ferrites [Innui and Ogasawaka, 1978]. The increase in intrinsic coercivity with decrease in grain size has two possible contributions, one affecting the nucleation of reverse domains and the other affecting the growth of reverse domains.

Nucleation of reverse domains are most likely at surface defects or at sites where the local anisotropy is lowered. Brown (1963) has shown that the number of defects per unit surface area decreases rapidly with decreasing grain size. Thus, a smaller grain size implying a smaller surface area for a given grain would increase the coercivity by decreasing the nucleation probability. Growth of reverse domains can be effectively impeded by grain boundaries since grain boundaries constitute regions of local decrease in exchange energy and anisotropy and hence, lowered domain wall energy. Thus a smaller grain size would provide more grain boundary area to pin domain walls and impede the growth of reverse domains. This would also contribute to an increase in the coercivity.

The invariance of the intrinsic coercivity with

composition suggests that the coercivity is insensitive to the relative amounts of fcc and hcp phases and to the overall fault density. (As discussed earlier, increases in fcc phase content was accompanied by an overall increase in fault density.) Lorentz electron microscopy revealed that domain walls can be pinned by faults in the fcc phase. This, in principle, would lead to an increase in the coercivity. However, the observed insensitivity of the macroscopically measured intrinsic coercivity to the fault density and the ease of unpinning from the faults under the low applied fields in the electron microscope, suggest that pinning effects by the faults constitute a minor contribution to the coercivity.

In summary, the addition of Cr has varied effects on the microstructure and magnetic properties of Co-Cr alloys. While Cr additions enhance the fcc phase retention and subsequently the fault density, they cause a decrease in grain size. The additions also decrease saturation magnetization. Furthermore, the intrinsic coercivity is fairly insensitive to Cr additions for a given grain size and the coercivity increases with decreasing grain size. It can thus be seen that several simultaneous microstructural and magnetic changes result from Cr additions.

5. CONCLUSIONS.

The major findings of this study of the microstructure and magnetic properties of Co-Cr alloys are the following:

1. The addition of Cr to Co was found to stabilize the fcc phase. This was attributed to the lowering of the martensitic start temperature, M_S.

2. Chromium additions were found to decrease the average grain size of these binary alloys probably by enhancing the nucleation rate during recrystallization.

3. The intrinsic coercivity for a given composition was found to increase with decreasing grain size. This was attributed to the decrease of nucleation sites for reverse domains and to the increase in grain boundary area acting as pinning sites for domain wall motion.

4. Lorentz microscopy revealed that the stacking faults in the fcc phase and grain boundaries acted as pinning sites. The latter were observed to be more effective pinning sites than the former.

ACKNOWLEDGEMENTS

I would like to express my appreciation to Professor G.Thomas for his encouragement and support through the course of this work. I am also grateful to Professors E.Weber and D. Hess for reviewing this work.

I am very grateful to Dr. J.S. Gau for providing the samples and magnetic measurements for this study and for his active interest in this work. I would also like to thank Mr. D. Jurica for his care and maintenance of the microscope facilities and for all his help.

I would like to express my appreciation for my parents for their understanding and support. I am very grateful to my brother Kai, for his words of encouragement and for always being there when I have needed it.

I am indebted to my fellow graduate students for their help through the course and completion of this work. I am very thankful to R. Ramesh for his interest in my work, for the many helpful discussions and for his advice and patience. I would like to express my deepest gratitude to K. Srikrishna for his friendship, (for calling me Ms. Chan) and for everything he has done to help me. Krishna... Muchas Gracias!

Reference

Allibert, C. Bernard, C., Valignat, N., Dombre,M. J.Less-Common Met.59, (1978) 211.

Bitter, F., Phys. Rev. 38, (1931) 1903.

Brown, W.F. Micromagnetics, London and N.Y., John Wiley and Sons, (1963) 66.

Bolzoni, F., Leccabue,F., Panizzieri, and Pareti, L., J.M.M.M., 33-34, (1983) 845-846.

Chen, C., Magnetism and Metallurgy of Soft Magnetic Materials, Dover, N.Y., (1986) 200.

Chikazumi, S., Physics of Magnetism, John Wiley, (1964)

Craik, D.J., Tebble, R.S.,Ferromagnetism and Ferromagnetic Domains, North Holland, (1965)

Cullity, B.D., Introduction to Magnetic Materials , Addison - Wesley, Reading MA, (1978) 411.

Elsea, A., Westerman, A., and Manning, G., Trans. AIME, 180, (1949), 579.

Farcas, T. Ann Physique, 8, (1937) 146.

Grigor'ev, E., Yu-p'u, E. and, Sokolovskaya, E.Juss. J. Inorg. Chem., 6,(1961) 827.

Hansen, M., Constitution of Binary Alloys, 2nd edition McGraw-Hill, N.Y., (1958) 467.

Hashimoto,H., Howie,A., and Whelan, M.J., Proc. Roy. Soc. A269, (1962), 80.

Hitzenberger, C., Karnthaler, H., Korner, A., Phys. Stat. Sol.(a), 89, (1985), 133

Howard, J.K., J. Vac.Sci.. Tech.A., 4 (1986) 1.

Houska, C.R., Averbach, B.L. and Cohen, M., Acta Metall., 8 (1960) 81.

Innui, T., Ogasawara, N., J. Appl. Physics, 49(3), (1978) 2019.

Iwasaki, S., IEEE Trans. Magn., Mag-16 (1980) 71 .

Iwasaki, S., Nakamura, Y., IEEE Trans. Magn., Mag-13 (1977)

1272.

Iwasaki, S., Ouchi, K., IEEE Trans. Magn., Mag-14 (1978) 849.

Iwasaki, S., Ouchi, K., Honda, N., IEEE Trans. Magn., Mag-16 (1980) 1111.

Lin,I., Mishra, R., Thomas, G., IEEE Trans. Magn., 20 (1984) 134

Livingston, J., J. Appl. Physics, 52(3) 1981, 2544.

Livingston, J., Prog. Mater. Sci., 7, (1981), 243.

Mahajan, S., Green, M.L., Braun, D., Met. Trans A. 8A (1977) 283

McCurrie, R.A., Carswell, G.P., Phil. Mag. 23 (1970) 333.

Metcalfe, A.G., J. Metals, (1953), 357.

Nishiyama, Z., Martensitic Transformation, Academic Press, (1978) 48.

Okada, M. Ph.D. Thesis, Universitly of California, Berkeley, (1978)

Ouchi, K., Iwasaki, S., Digests of the Int. Mag. Conf. Tokyo, Japan (1987) CA-01.

Roebuck,B., Almond, E.A., Cottenden, A., Mat.Sci.Eng. 66 (1984) 179.

Sage, M., Guillaud, Ch, Rev. Met., 47, (1950)139.

Silcox, J. Phil. Mag., 8 (1963) 1395.

Watanabe, D. Int. Symp. on In-Situ Experiments of HVEM, Osaka Univ., (1985) 421.

White, R.M., Sci. Am. 243 (1980) 47.

Table 1

Sample: H4 15 at.% Cr

Grain boundary	at.% Cr	at.% Co
	20.11 ± 0.29	79.89 ± 0.65
	19.95 ± 0.25	80.05 ± 0.49
	19.82 ± 0.21	80.18 ± 0.49
	19.59 ± 0.21	80.41 ± 0.49
	19.88 ± 0.25	80.32 ± 0.49
	19.56 ± 0.28	80.44 ± 0.49
Grain interior	19.88 ± 0.25	80.32 ± 0.49
	19.51 ± 0.21	80.49 ± 0.49
	19.54 ± 0.21	80.46 ± 0.49

Table 2

Sample: H2 20 at.% Cr

Grain boundary	at.% Cr	at.% Co
	24.45 ± 0.40	75.55 ± 0.78
	24.48 ± 0.44	75.52 ± 0.78
	24.77 ± 0.45	75.23 ± 0.77
	24.78 ± 0.50	75.22 ± 0.93
	24.90 ± 0.50	75.10 ± 0.93

Grain interior	at.% Cr	at.% Co
	24.31 ± 0.35	75.69 ± 0.62
	24.94 ± 0.32	75.06 ± 0.62
	24.98 ± 0.45	75.02 ± 0.77
	24.42 ± 0.35	75.58 ± 0.62
	25.16 ± 0.55	74.84 ± 1.08
	24.20 ± 0.40	75.80 ± 0.80

Sample H2: 5 at.% Cr

Grain Boundary	at.% Cr	at. % Co
	7.55 ± 0.30	92.45 ± 0.93
	7.44 ± 0.26	92.56 ± 0.93
	7.38 ± 0.29	92.62 ± 0.93
	7.46 ± 0.31	92.54 ± 0.93
	7.08 ± 0.21	92.92 ± 0.94

Grain Interior	at.% Cr	at. % Co
	7.33 ± 0.25	92.68 ± 0.75
	7.28 ± 0.26	92.72 ± 0.75
	7.41 ± 0.22	92.59 ± 0.75

Figure Captions

Fig.1. The Co-Cr phase diagram (after Hansen)

Fig.2. The Co-Cr phase diagram (after Grigor'ev et. al.)

Fig.3. Schematic illustration of the observations of magnetic domains by out-of-focus method, showing that incident electron beams are deviated in opposite directions in adjacent interaction domains, leading to a deficiency of electrons at A, and an excess at B which appear to be imaginary domain walls.

Fig.4. [a],[b],[c],[d],and [e] X-ray diffraction spectra from H1 samples of compositions 1.44, 5, 10, 15.2 and 20 at.% Cr, respectively. [f] is the standard x-ray diffraction spectra from hcp and fcc Co.

Fig.5. X-ray diffraction spectra from H2 samples of compositions 1.44, 5, 10, 15.2, and 20 at.%Cr.

Fig.6. Plot of the ratio of fcc to hcp phase content in H2 samples.

Fig.7. X-ray diffraction spectra from H4 samples of compositions of 10 and 15 at.% Cr.

Fig.8. [a],[b],[c] are plots of saturation magnetization as function of Cr for samples of treatment H1, H2, and H3, respectively.

Fig.9. Plot of intrinsic coercivity as function of Cr content in H1 samples.

Fig.10. Plot of intrinsic coercivity as function of grain size for samples of 1.44 and 20 at.% Cr.

Fig.11. [a],[b],[c],[d],and [e] Optical micrographs of H1 samples of 1.44, 5, 10, 15.2, and 20 at.% Cr, respectively.

Fig.12. [a],[b],[c],[d],and [e] Optical micrographs of H2 samples of 1.44, 5, 10, 15.2, and 20 at.% Cr, respectively.

Fig.13. [a],[b],[c],[d],and [e] Optical micrographs of H3 samples of 1.44, 5, 10, 15.2, and 20 at.% Cr, respectively.

Fig.14. Plot of average grain size as function of Cr content in H2 samples.

Fig.15. [a] and [b] Optical micrographs of H4 samples of 10 and 15 at.% Cr, respectively.

Fig.16. Bright field micrograph of a H1 sample of 15 at.%Cr depicting the general microstructure of quenched alloys of Cr content of 5 at.% Cr or greater.

Fig.17. Bright field/dark field (BF/DF) pair of stacking faults in the hcp phase imaged on a [1 $\bar{2}$10] zone axis. The dark field of the faults was imaged using a streak along [0001] direction.

Fig.18. Bright field micrograph of faults in the fcc phase imaged on a [101] zone, using a 020 reflection.

Fig.19. Schematic figure depicting the effect of fault orientation on the diffraction pattern for a [112]

zone containing faults on all {111} planes.

Fig.20. BF/DF pair of faults in the fcc phase imaged on a [001] zone axis, showing the intrinsic nature of the faults.

Fig.21. Bright field micrograph of a two phase region and the corresponding diffraction patterns, showing the variants present and their relationships.

Fig.22. Bright field micrograph from a H1 sample of 1.44 at.% Cr showing the facetted interface between two hcp variants. [a] and [c] are diffraction patterns from the two hcp variants. [b] is the diffraction pattern from the interface.

Fig.23. BF/DF pair from a H1 sample of 1.44 at.% Cr showing faulting in the hcp phase. The foil orientation is [1 $\bar{2}$10]. The DF micrograph was formed using the streak along the [0001] direction.

Fig.24. BF/DF pair from a H1 sample of 1.44 at.% Cr. The foil orientation is [$\bar{1}$2 $\bar{1}$3]. The BF and DF images were formed using $\mathbf{g}$= 01 $\bar{1}$ $\bar{1}$, and $\mathbf{g}$= 0 $\bar{1}$11 reflections, respectively.

Fig.25. BF image of the microstructure of H4 samples of 15at.%Cr depicting that the fault density has decreased after equilibrium treatment.

Fig.26. Bitter powder domain pattern observed on the basal plane of 1.44 at% Cr under an applied normal field of ~1KOe.

Fig.27. Schematic diagram of [a] wavy pattern of oppositely magnetized regions and of [b] spike magnetic domain patterns.

Fig.28. Bitter powder domain pattern observed from a sample of 15 at.%Cr. [a] Easy axis of magnetization is in the plane of the sample surface (for the left grain). [b] Easy axis of magnetization is normal to the sample surface.

Fig.29. Bitter powder domain pattern showing the formation of spike domains at the grain boundaries.

Fig.30. Bitter powder domain pattern from a highly faulted sample, illustrating the complexity of such patterns and the subsequent difficulty in interpreting them.

Fig.31. Lorentz electron micrograph from a H1 sample of 5 at.%Cr showing stripe magnetic domains. The foil orientation is [2 $\bar{4}$23].

Fig.32. Lorentz electron micrograph showing magnetic domains from a region containing both fcc and hcp phases.

Fig.33. Lorentz electron micrograph showing cross-tie walls in a thin region of the sample (near the edge of the sample).

Fig.34. Sequence of Lorentz electron micrograph showing interaction between the domain walls and faults. For details see text.

Fig.35. Lorentz electron micrograph showing the reversible wall motion inside the grains. For details see text.

Fig.36. Lorentz electron micrograph showing a domain wall pinned at the grain boundaries between grain 1 and grain 2.

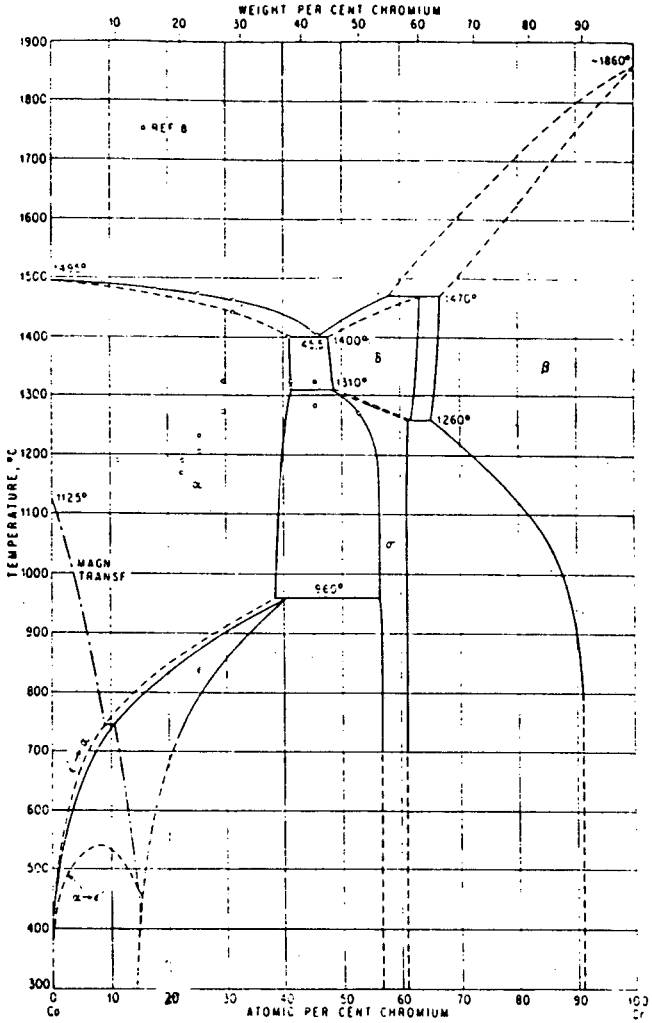

Fig. 1

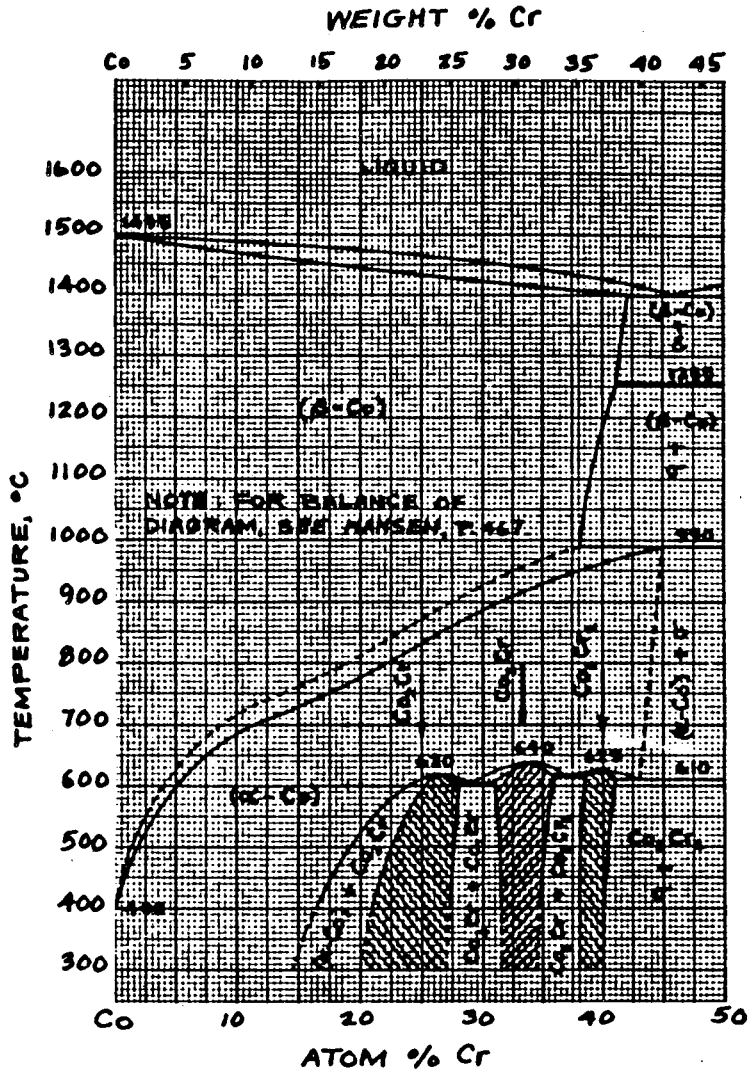

XBL 877-3388

Fig. 2

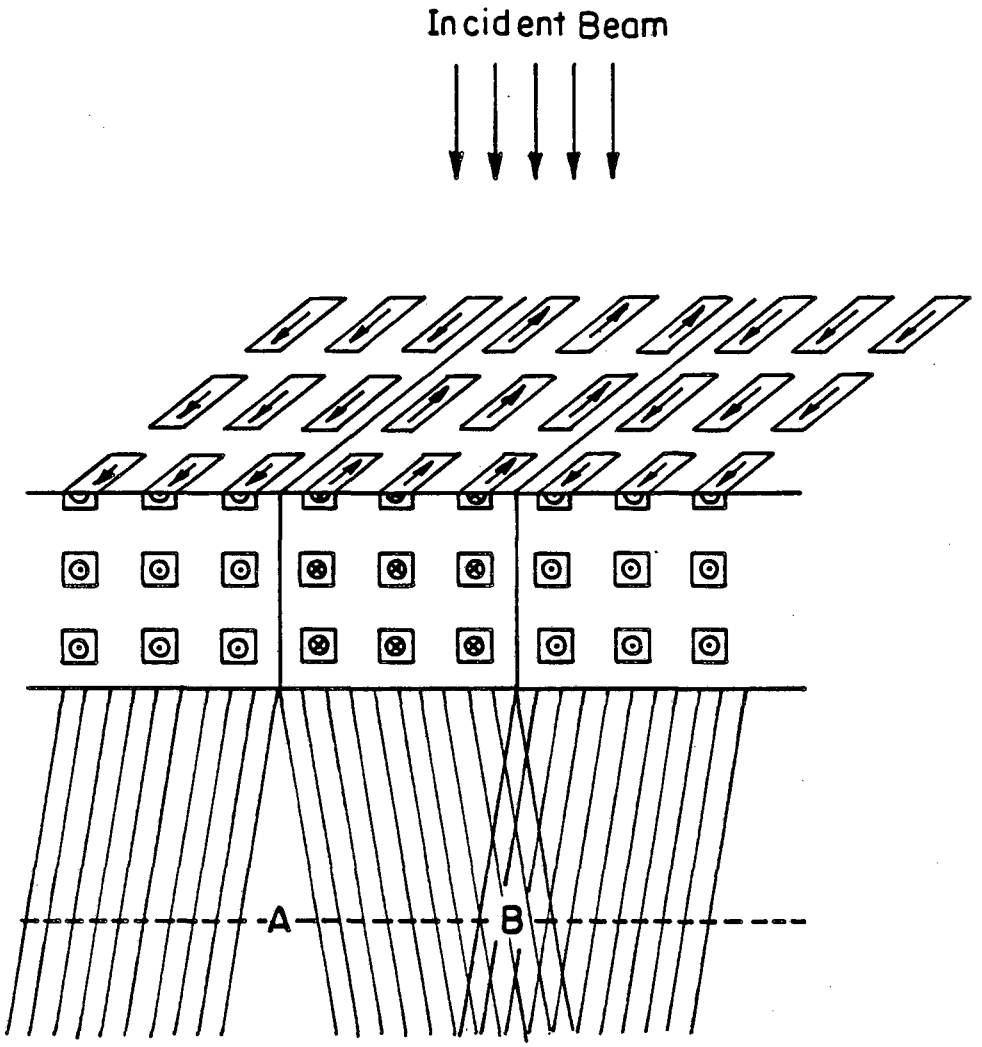

XBL 785-4985

Fig.3

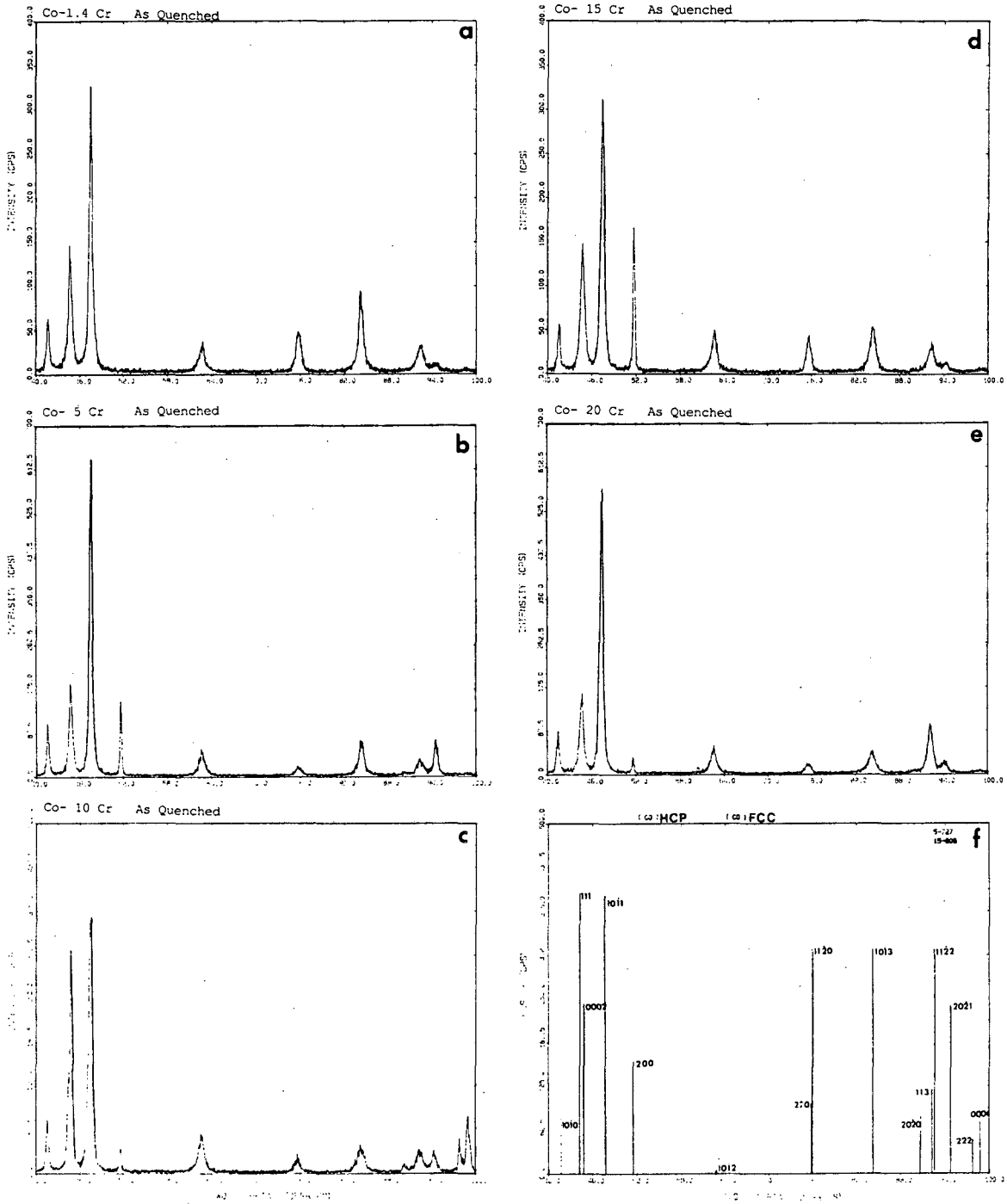
Co-1.4 Cr As Quenched
a
Co- 15 Cr As Quenched
d
Co- 5 Cr As Quenched
b
Co- 20 Cr As Quenched
e
Co- 10 Cr As Quenched
c
(ω):HCP (ω):FCC
f
111
1011
0002
200
1010
1012
220
1120
1013
113
2020
1122
2021
222
0004

Fig. 4

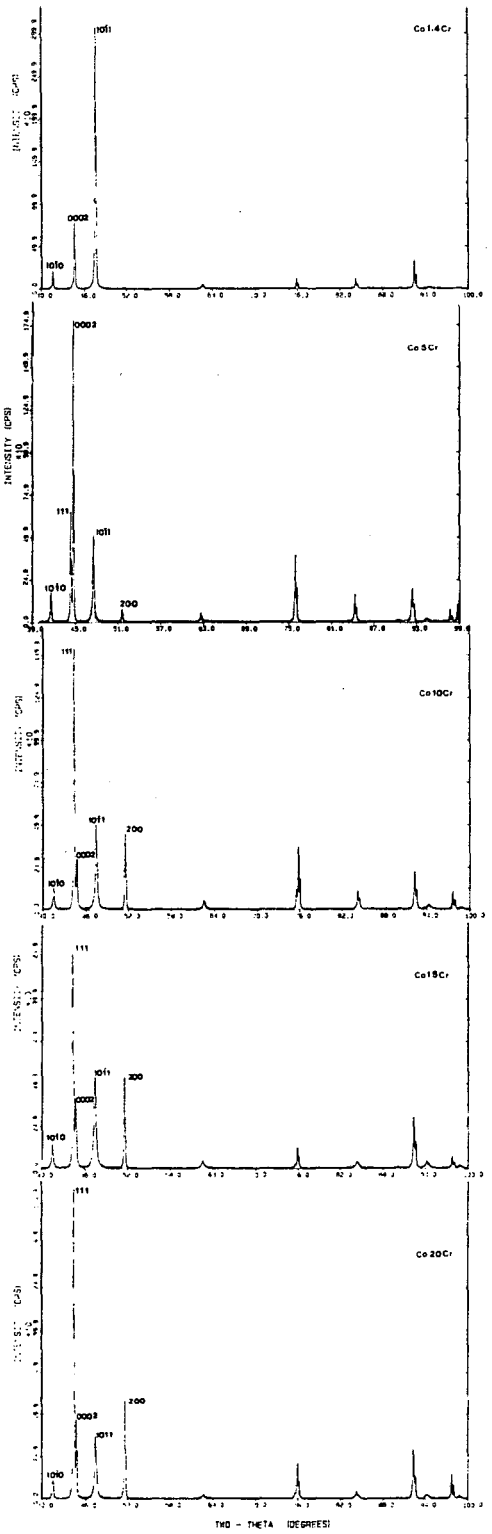

XBL 877-3180

Fig. 5

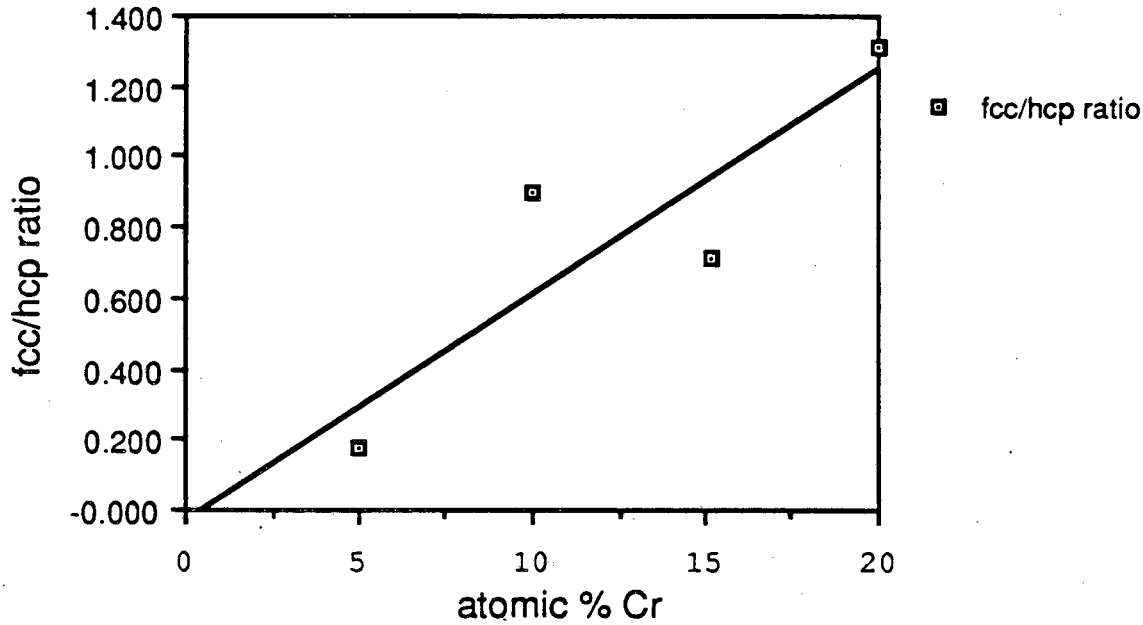

XBL 878-3686

Fig. 6

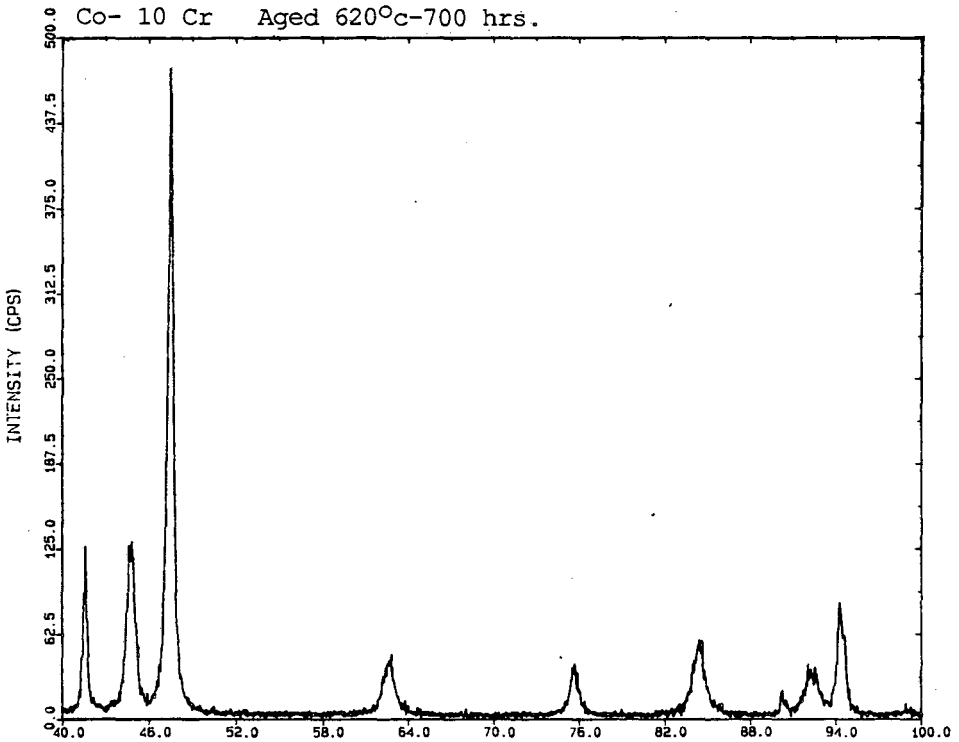
Co- 10 Cr Aged 620°c-700 hrs.
INTENSITY (CPS)
0.0
62.5
125.0
187.5
250.0
312.5
375.0
437.5
500.0
40.0
46.0
52.0
58.0
64.0
70.0
76.0
82.0
88.0
94.0
100.0

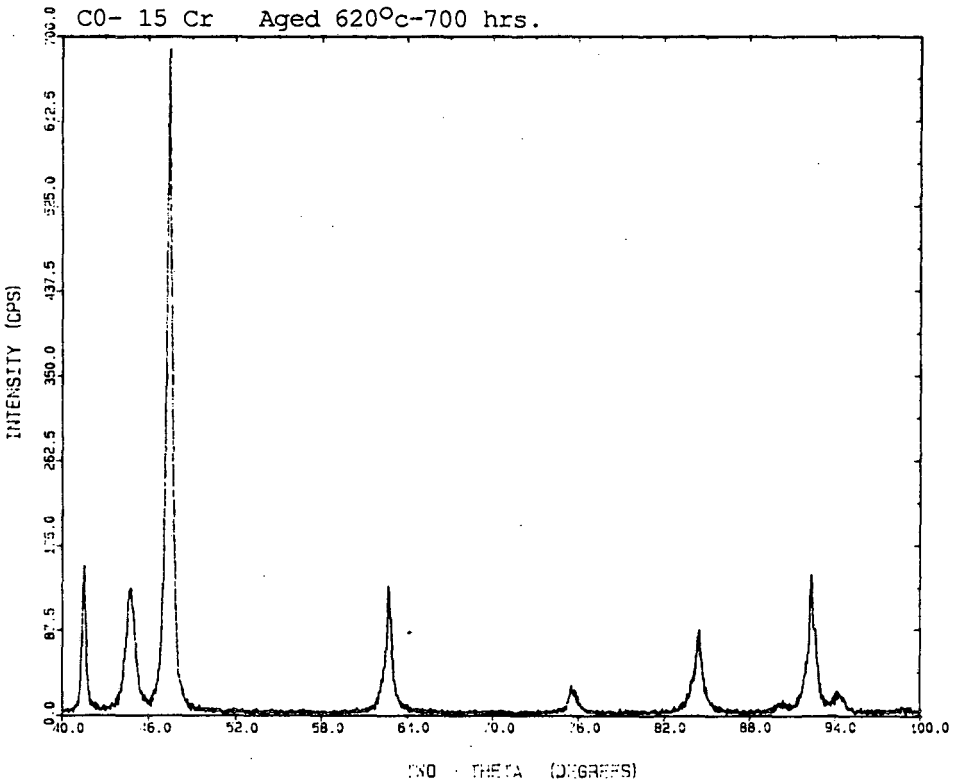
C0- 15 Cr Aged 620°c-700 hrs.
INTENSITY (CPS)
0.0
87.5
175.0
262.5
350.0
437.5
525.0
612.5
700.0
40.0
46.0
52.0
58.0
64.0
70.0
76.0
82.0
88.0
94.0
100.0
TWO THETA (DEGREES)

Fig. 7

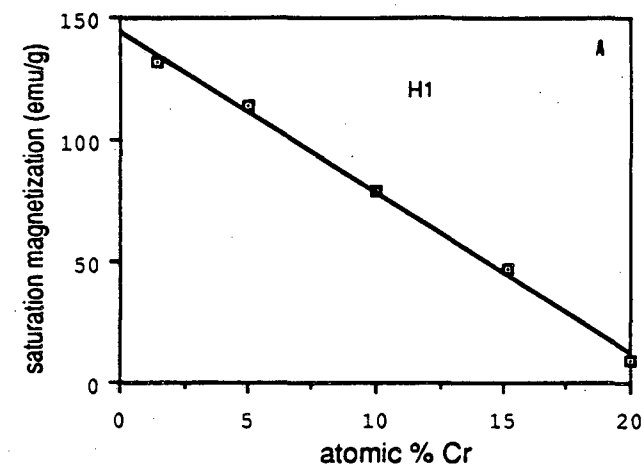

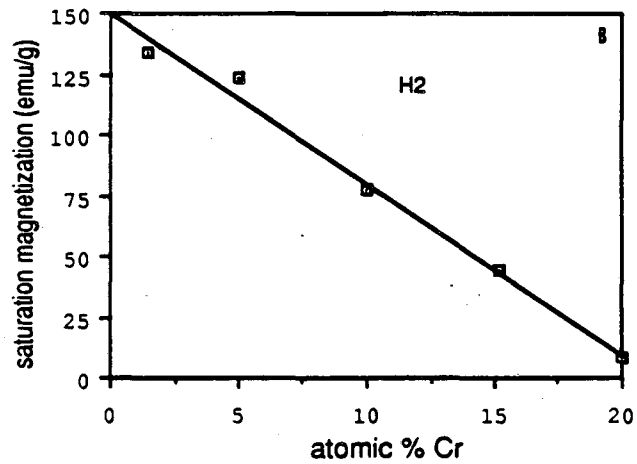

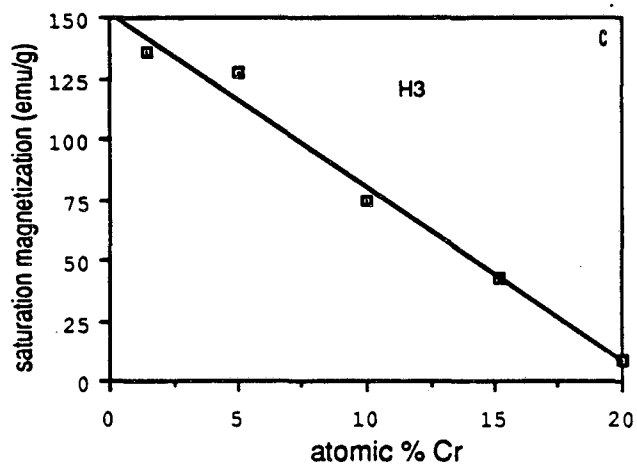

XBL 878-3687

Fig. 8

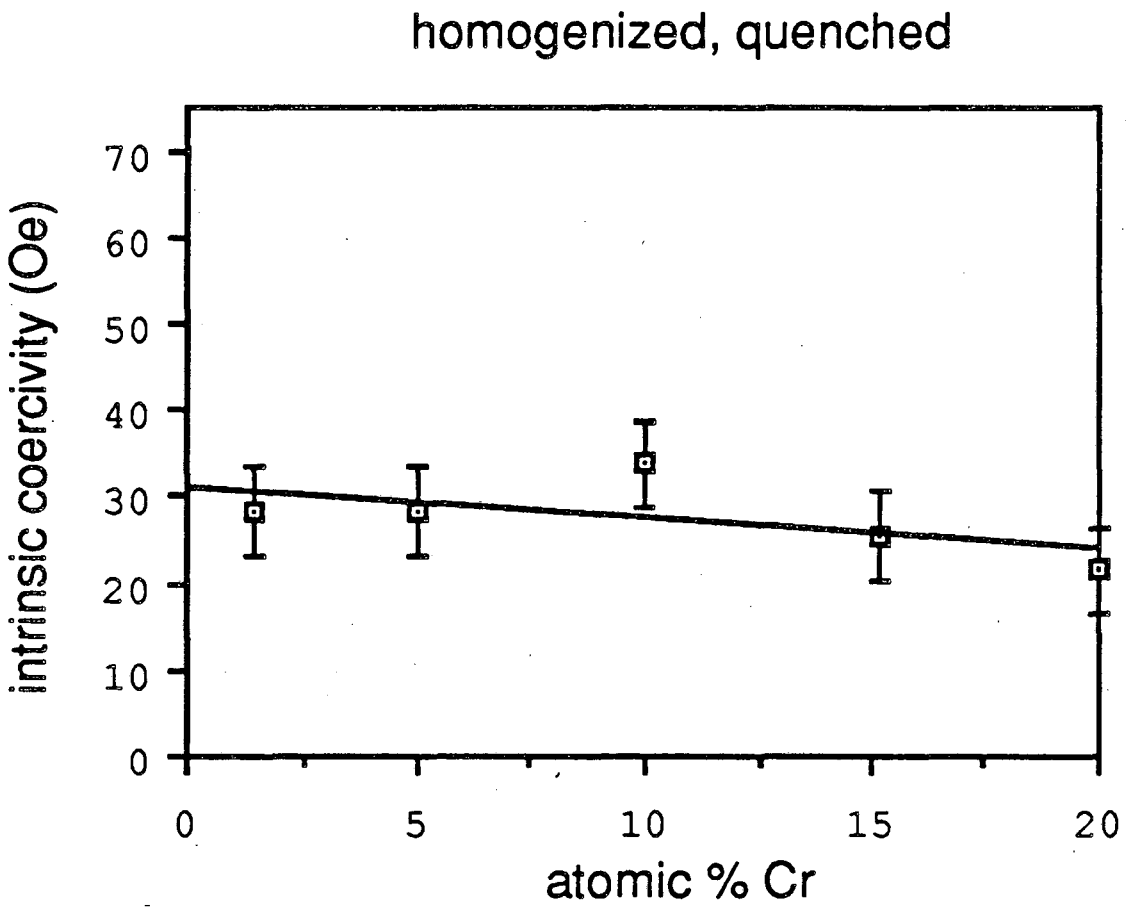

XBL 876-3000

Fig. 9

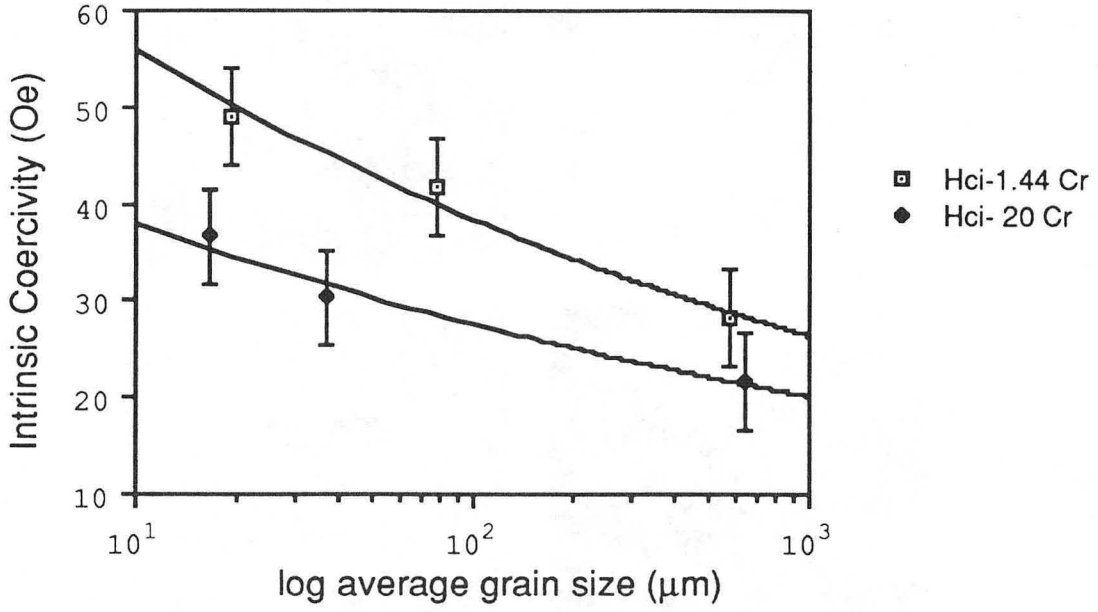

XBL 878-3688

Fig. 10

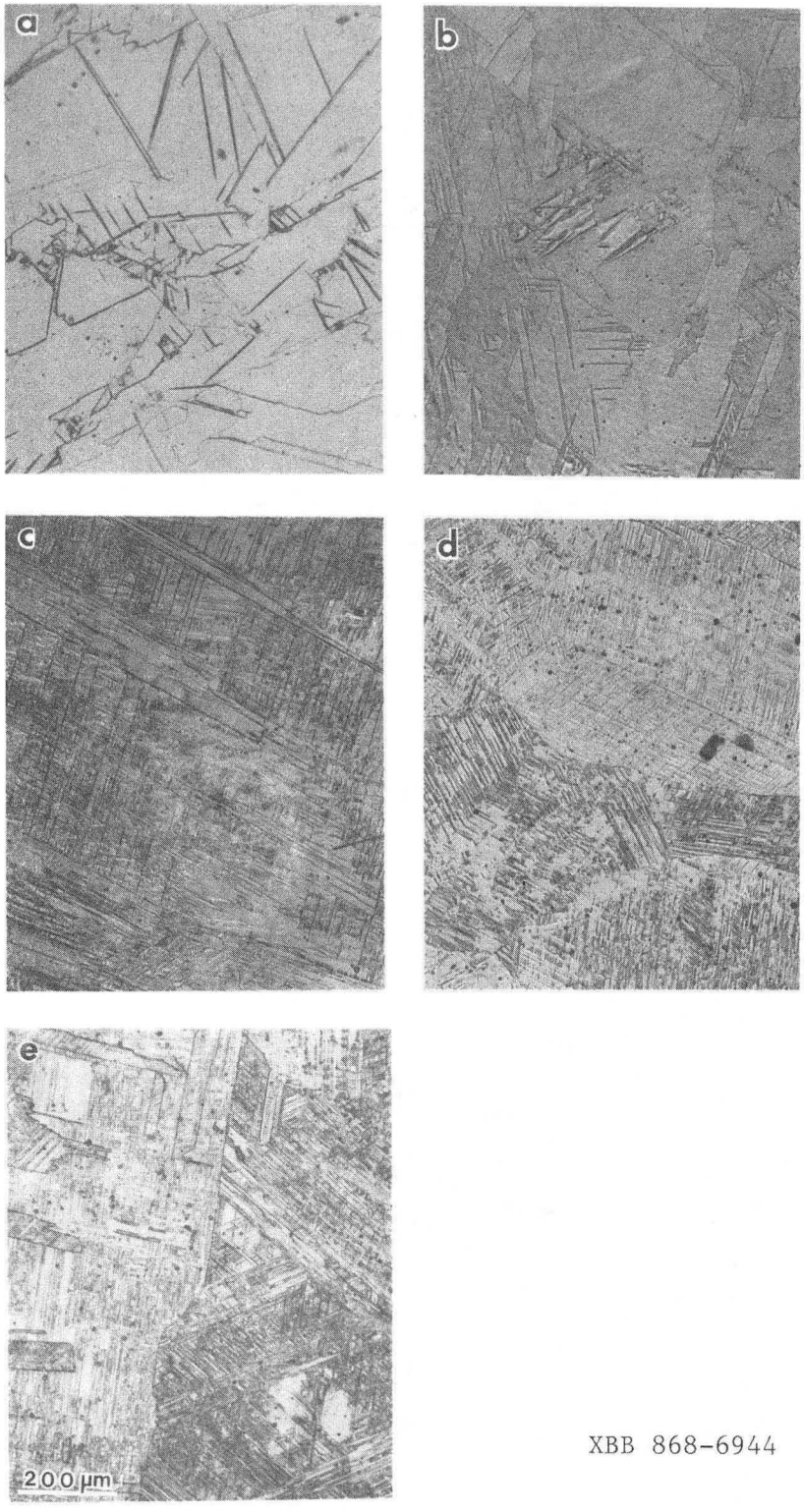

XBB 868-6944

Fig. 11

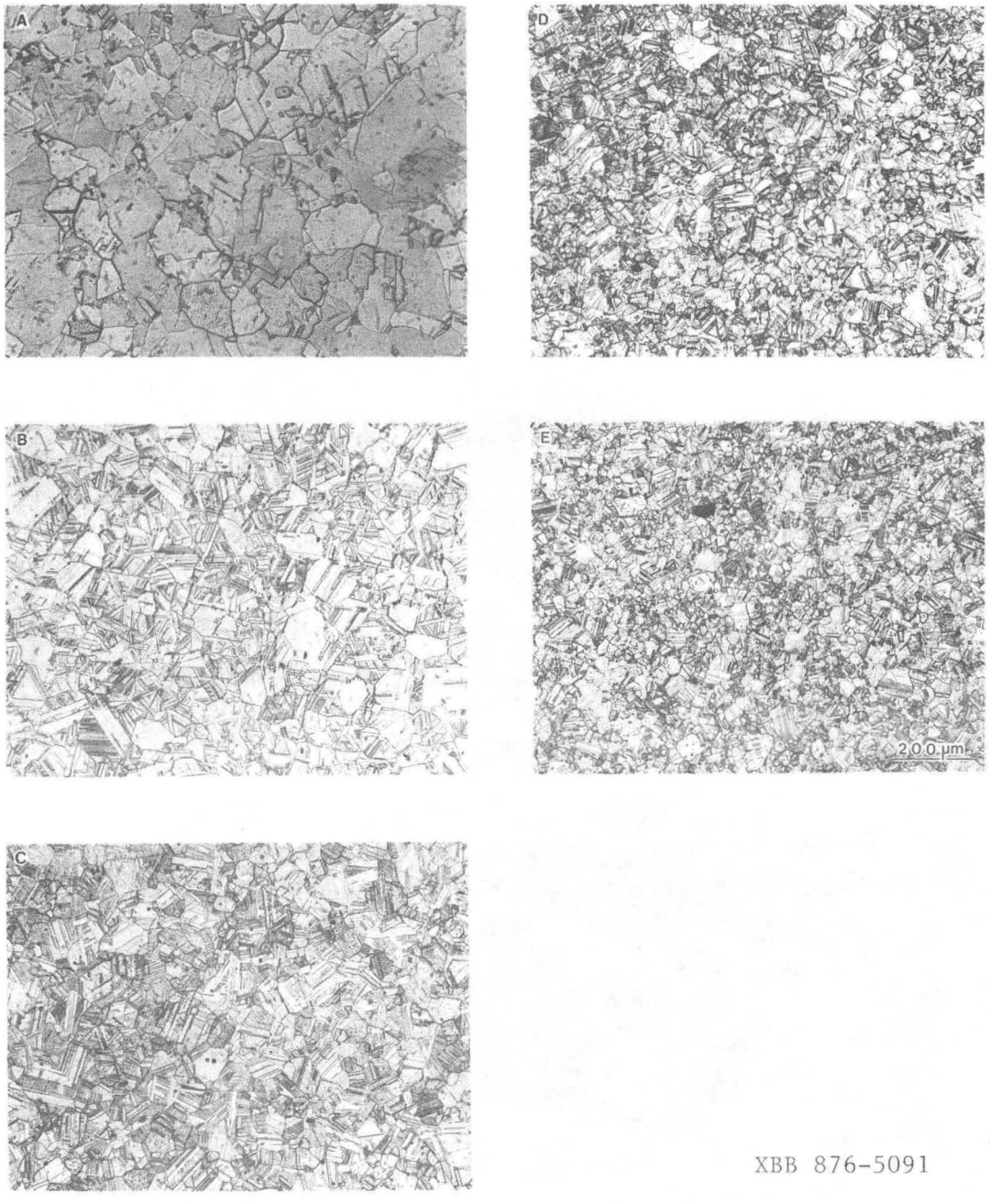

XBB 876-5091

Fig. 12

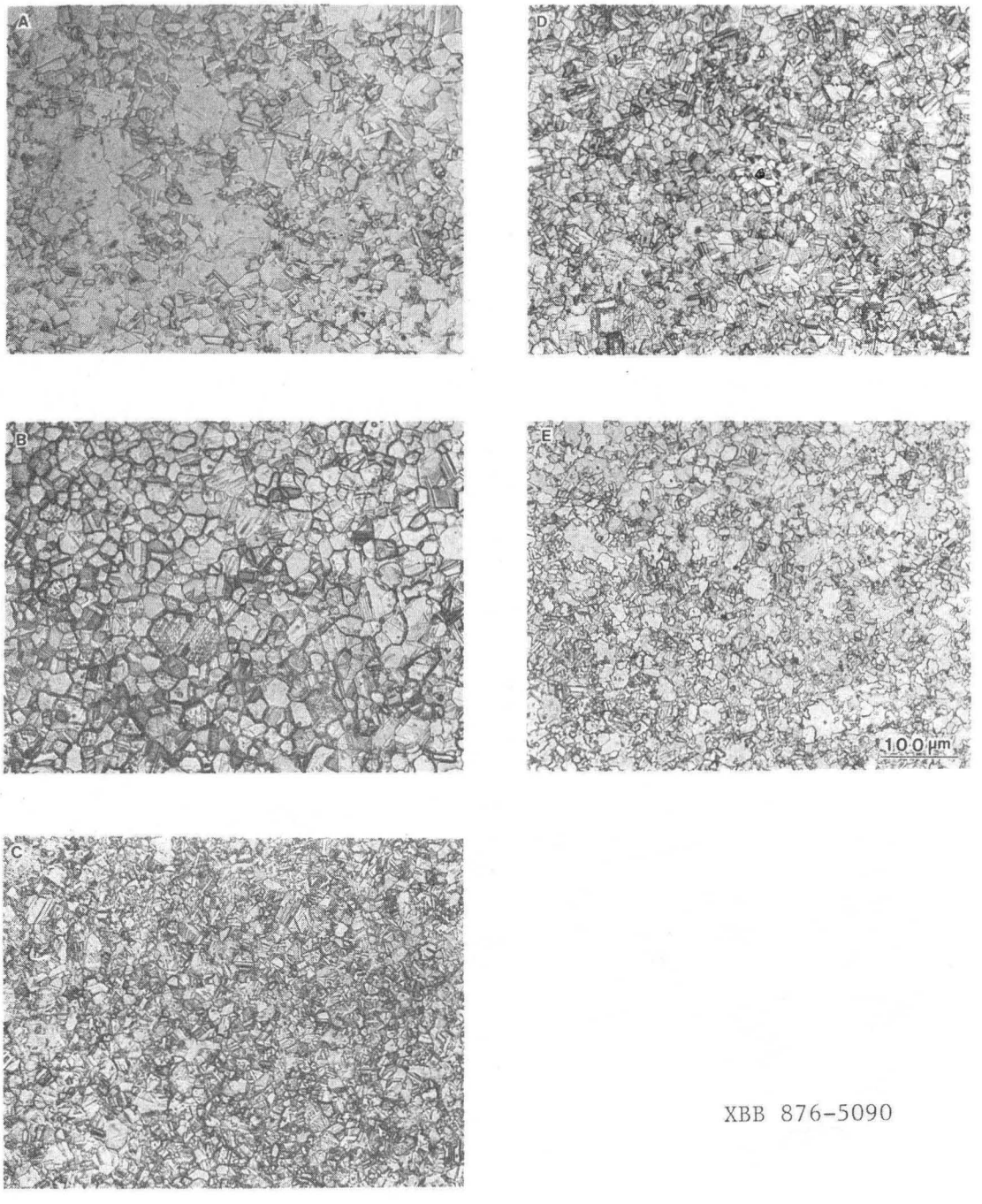

XBB 876-5090

Fig. 13

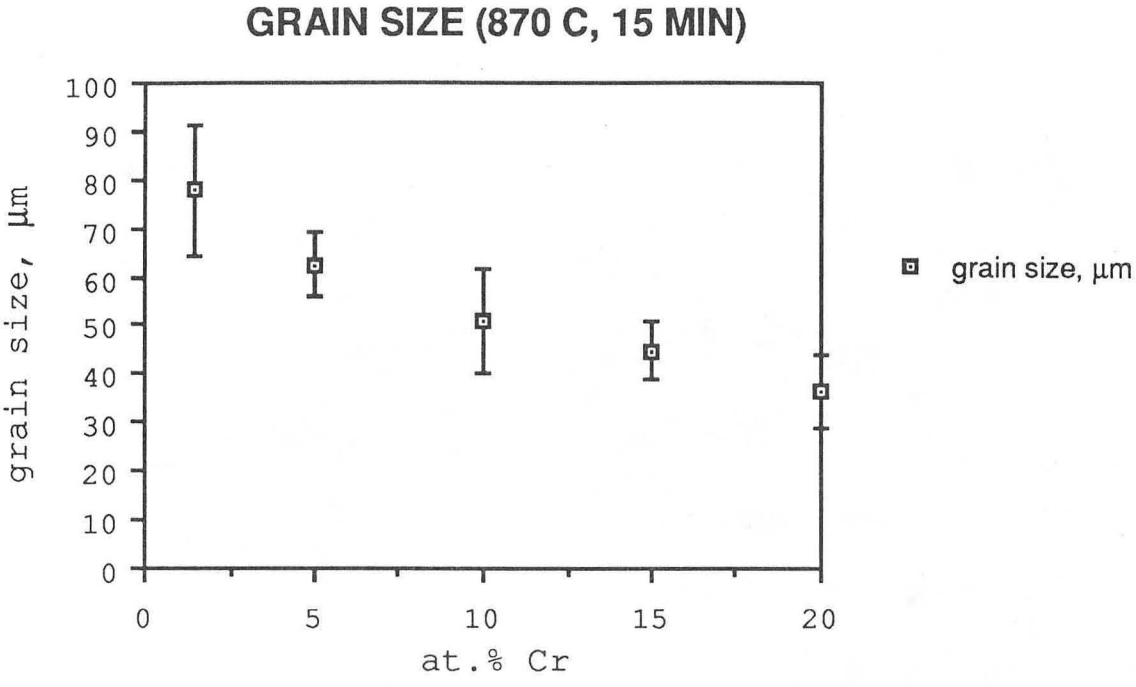

XBL 876-2861

Fig. 14

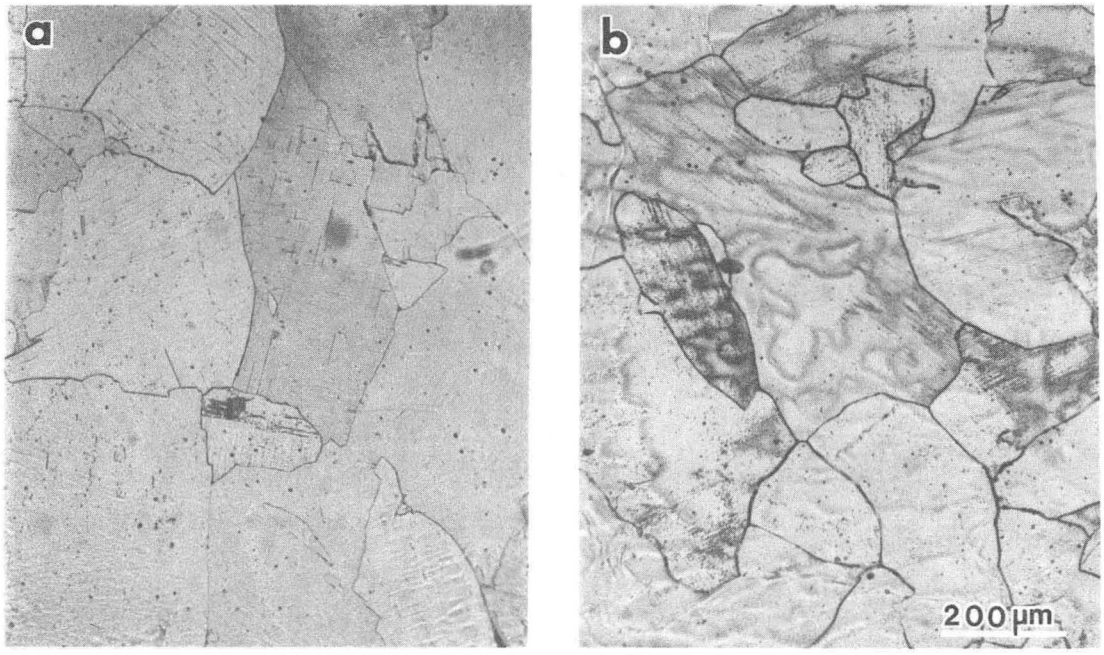

XBB 868-6943

Fig. 15

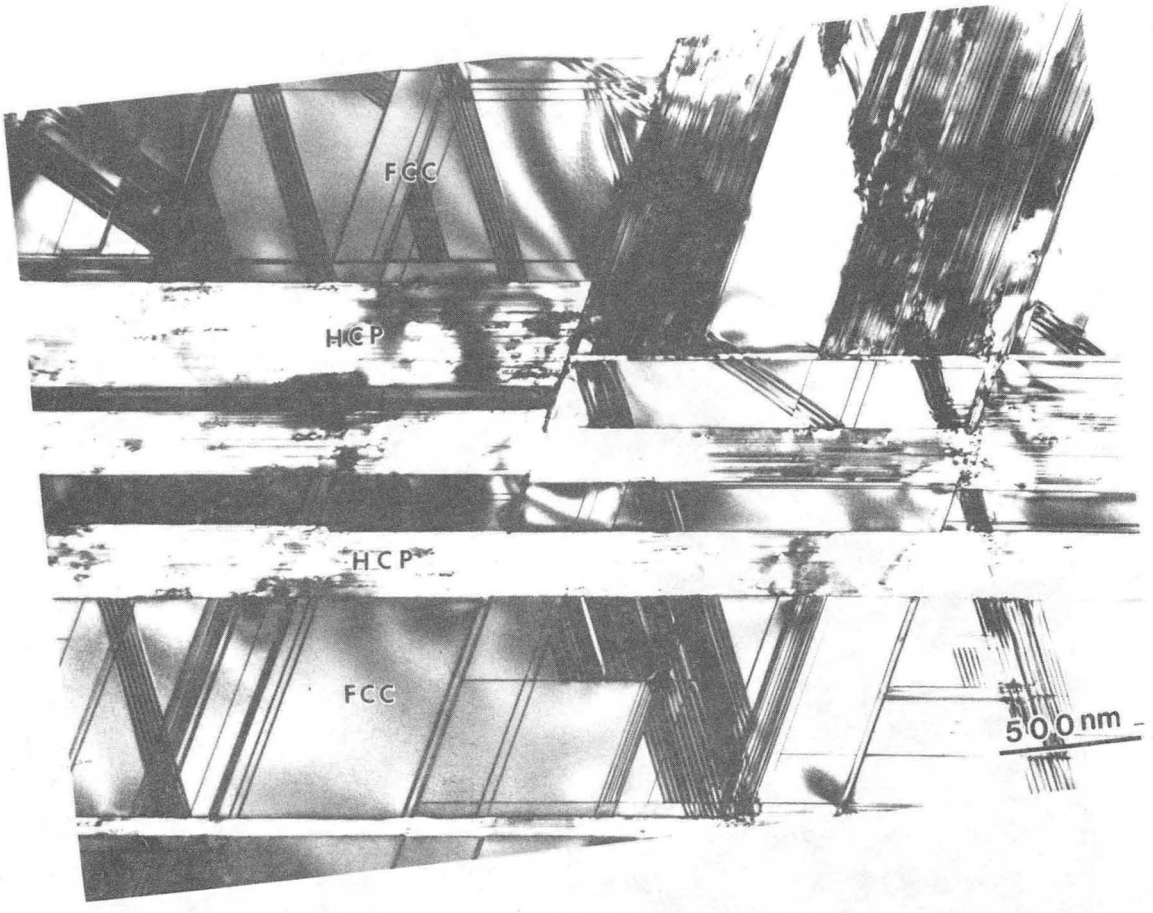

XBB 876-5087

Fig. 16

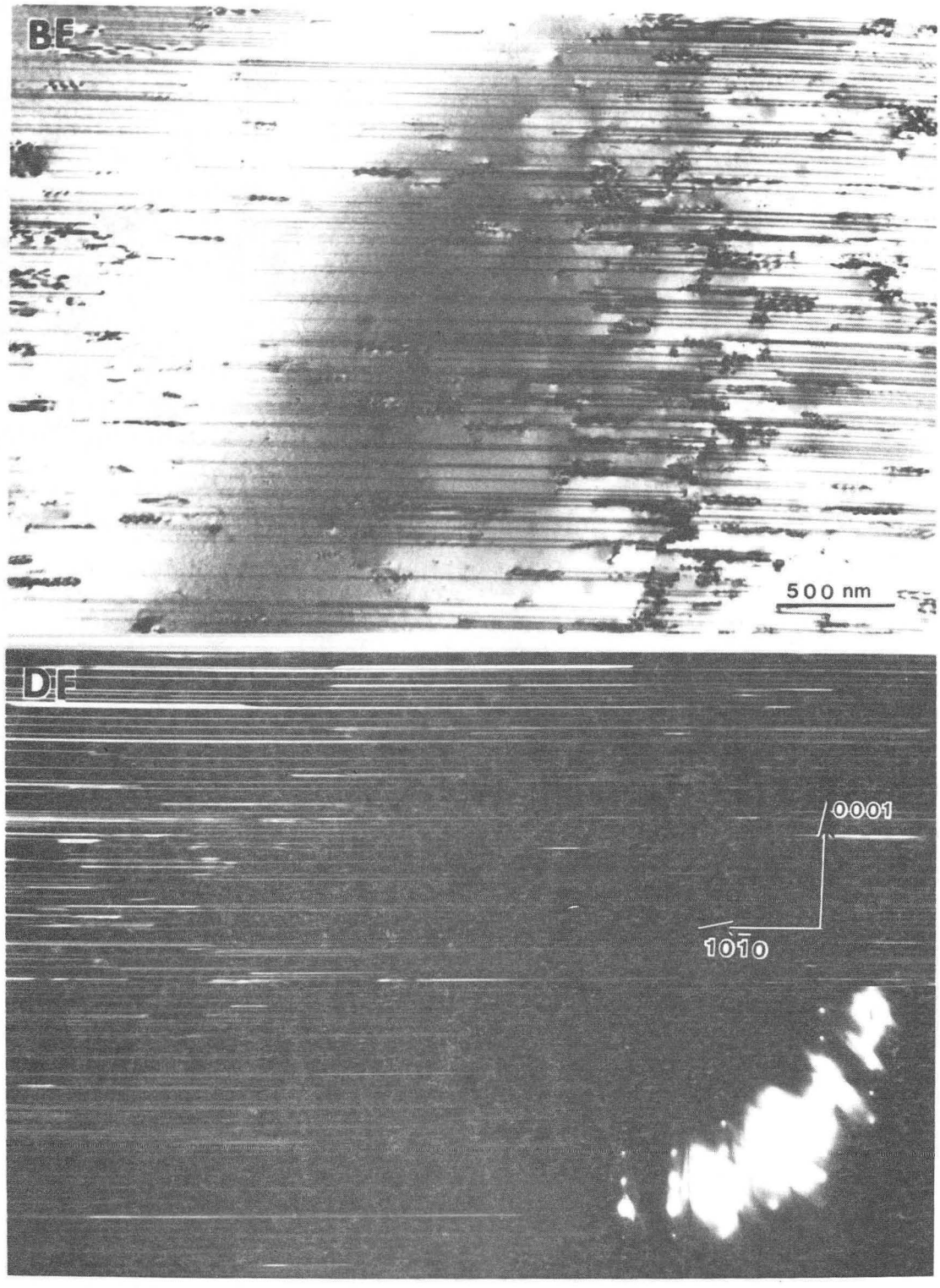

XBB 876-5096

Fig. 17

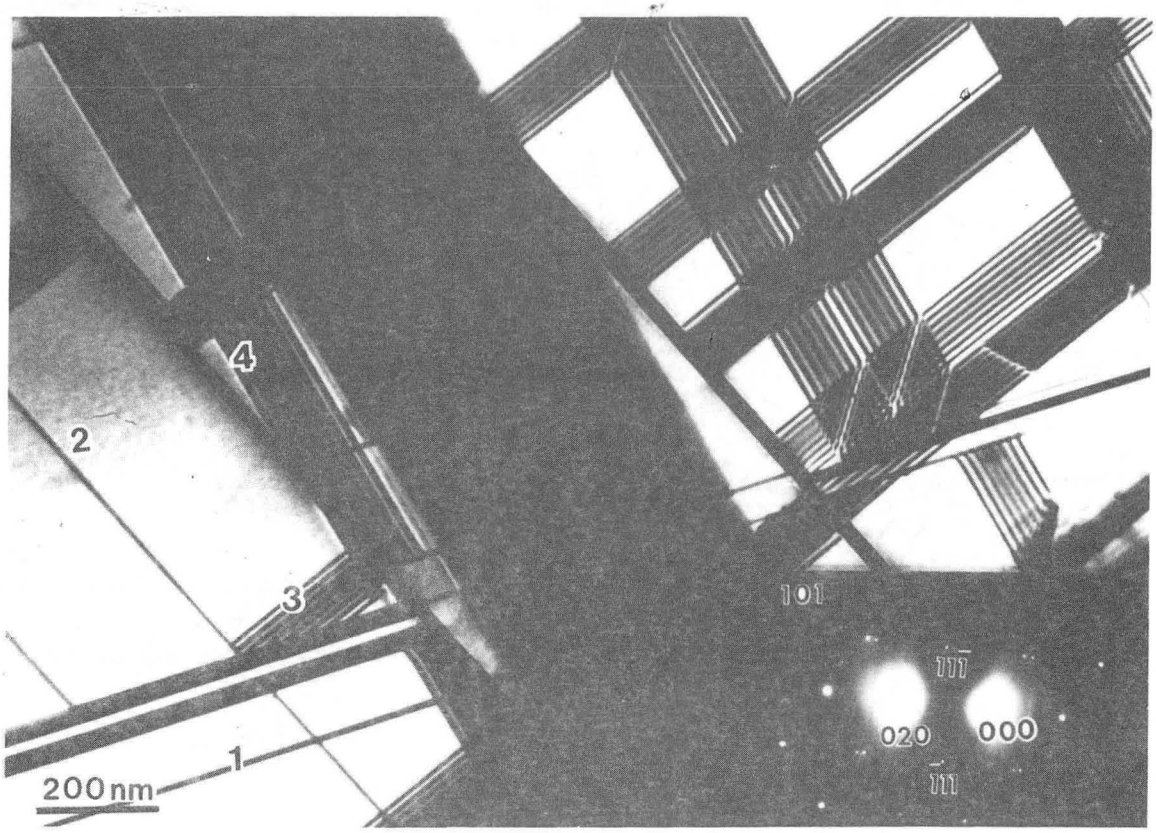

XBB 877-6397

Fig. 18

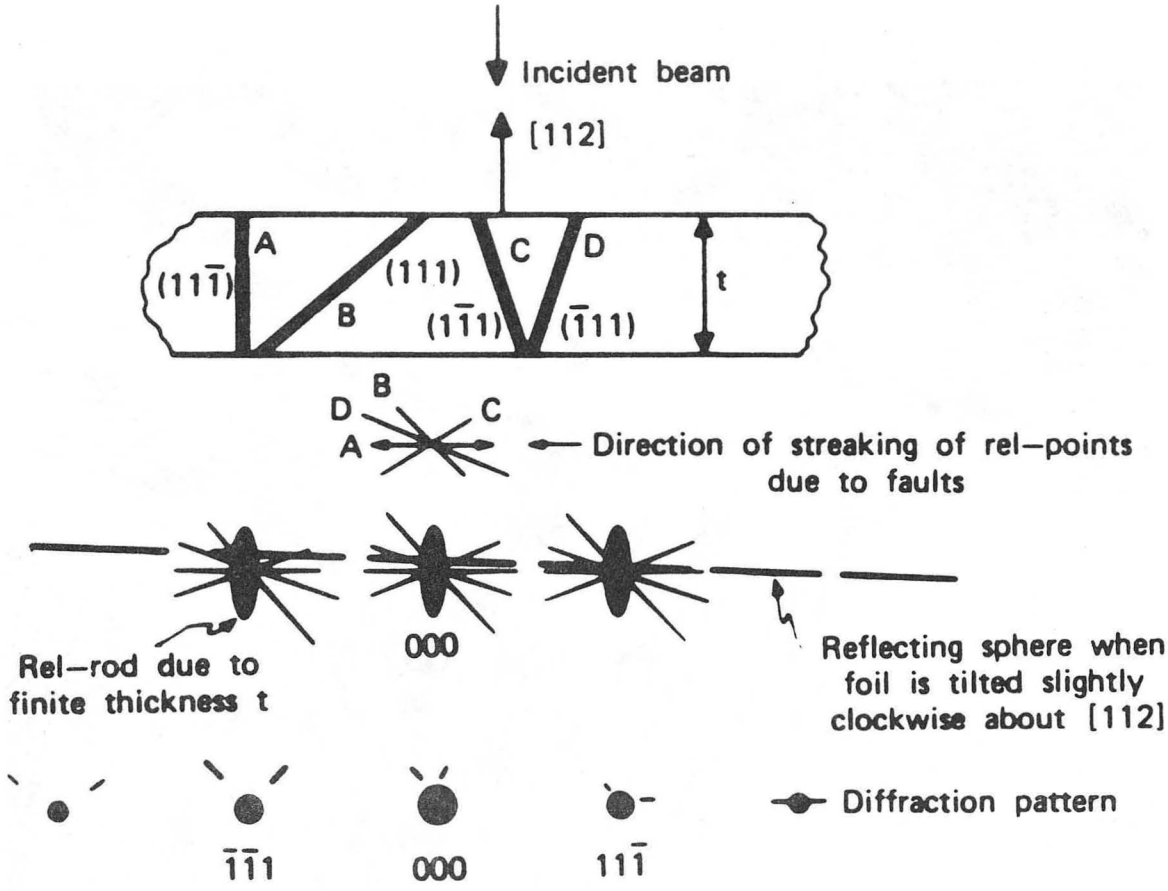

XBL 878-3689

Fig. 19

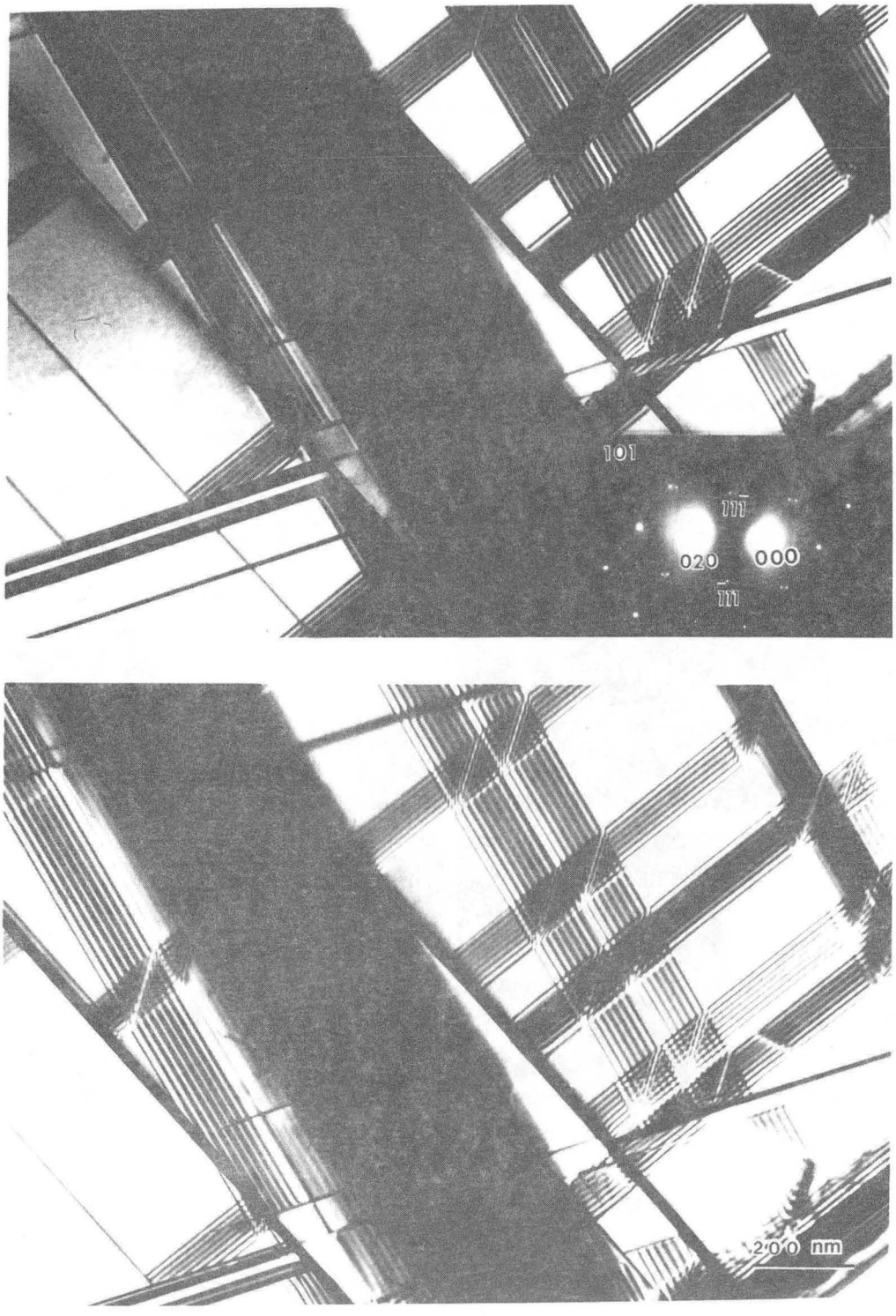

XBB 876-5099

Fig. 20

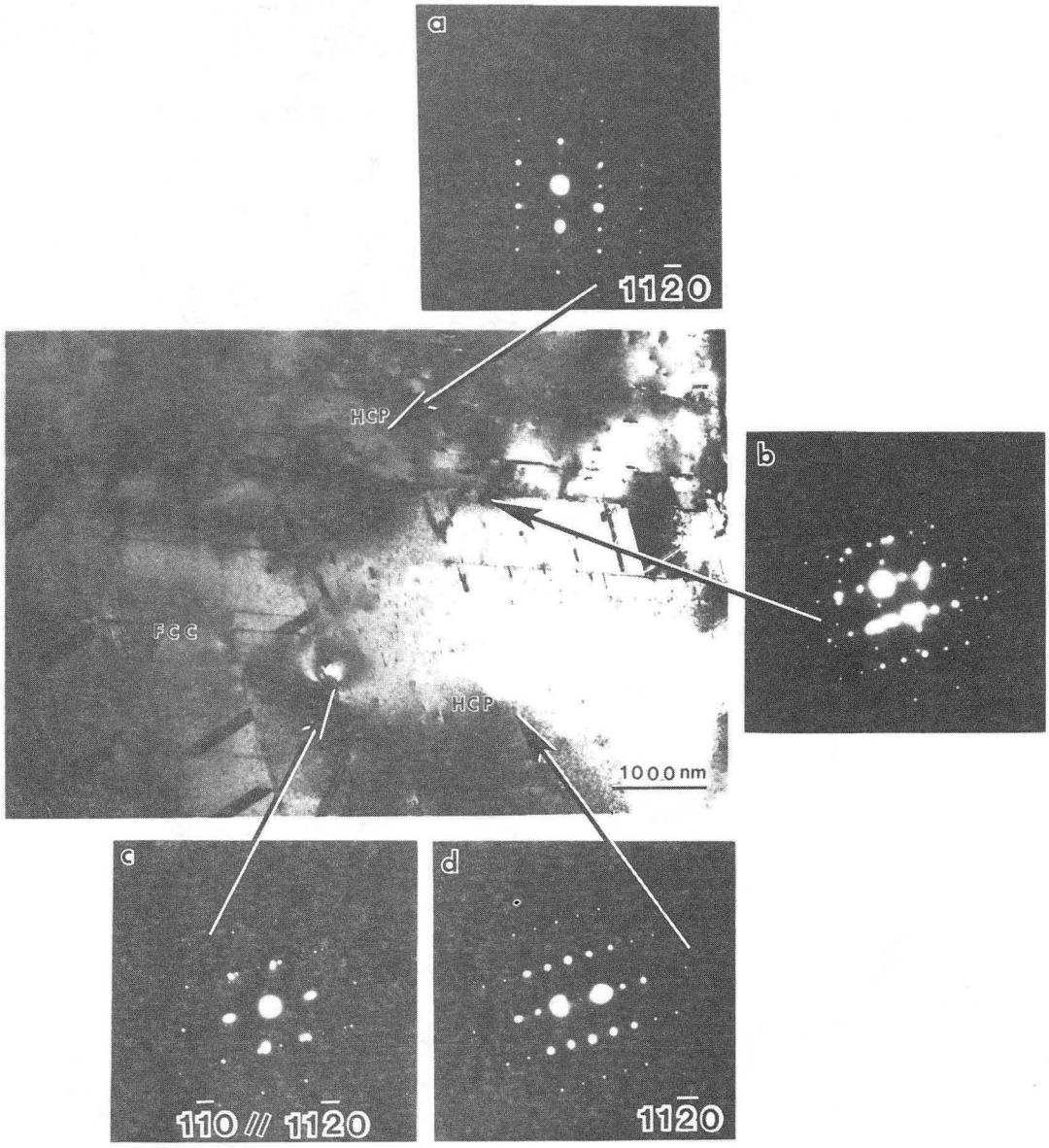

XBB 876-5411

Fig. 21

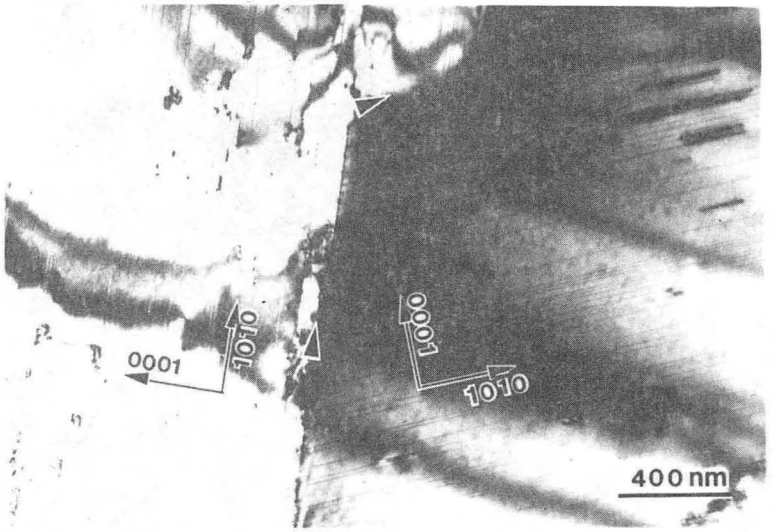

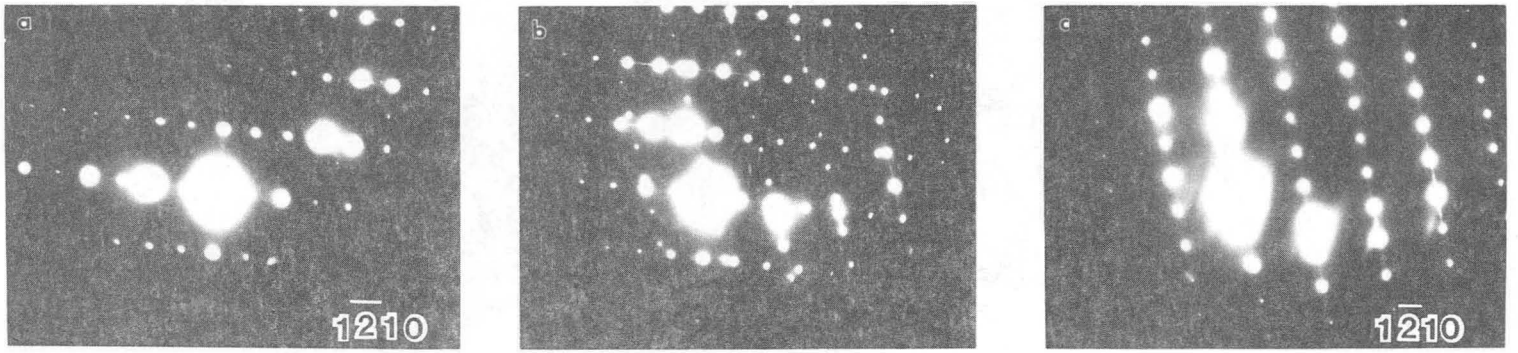

Fig. 22

XBB 876-5095

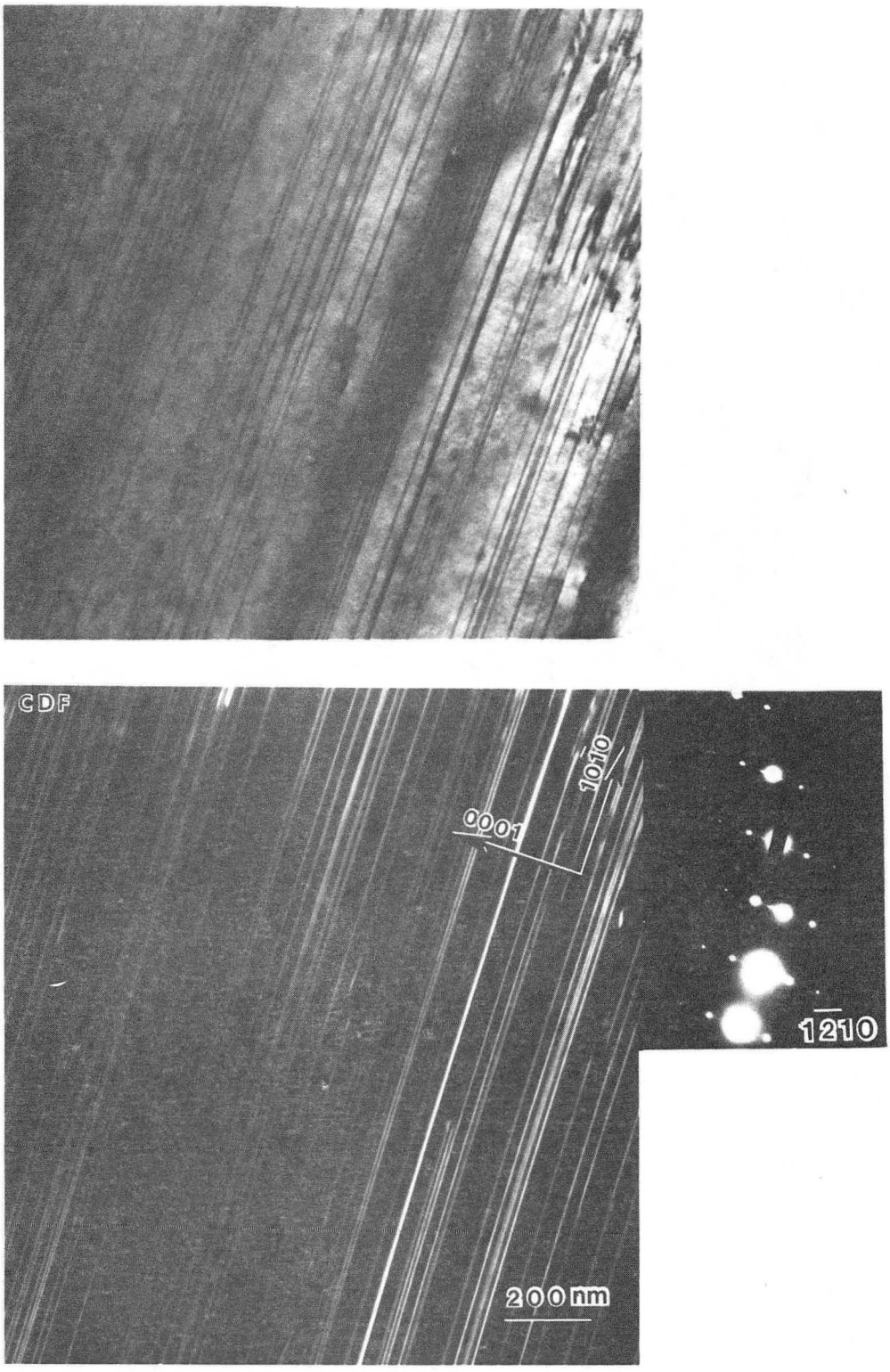

Fig. 23

XBB 876-5088

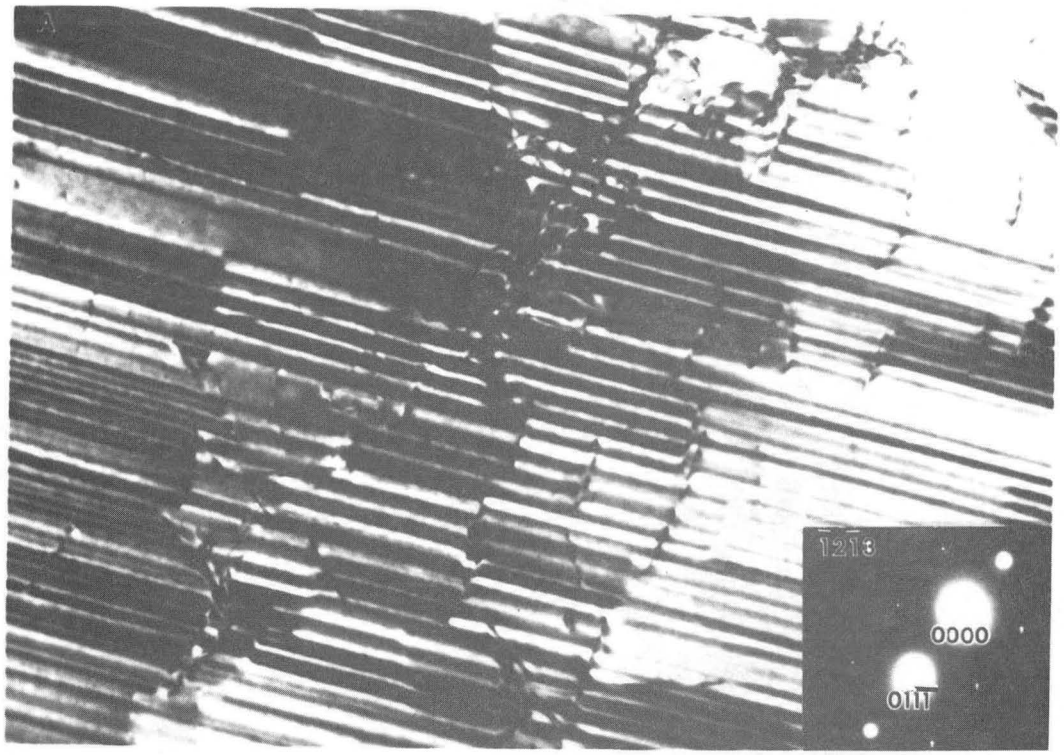

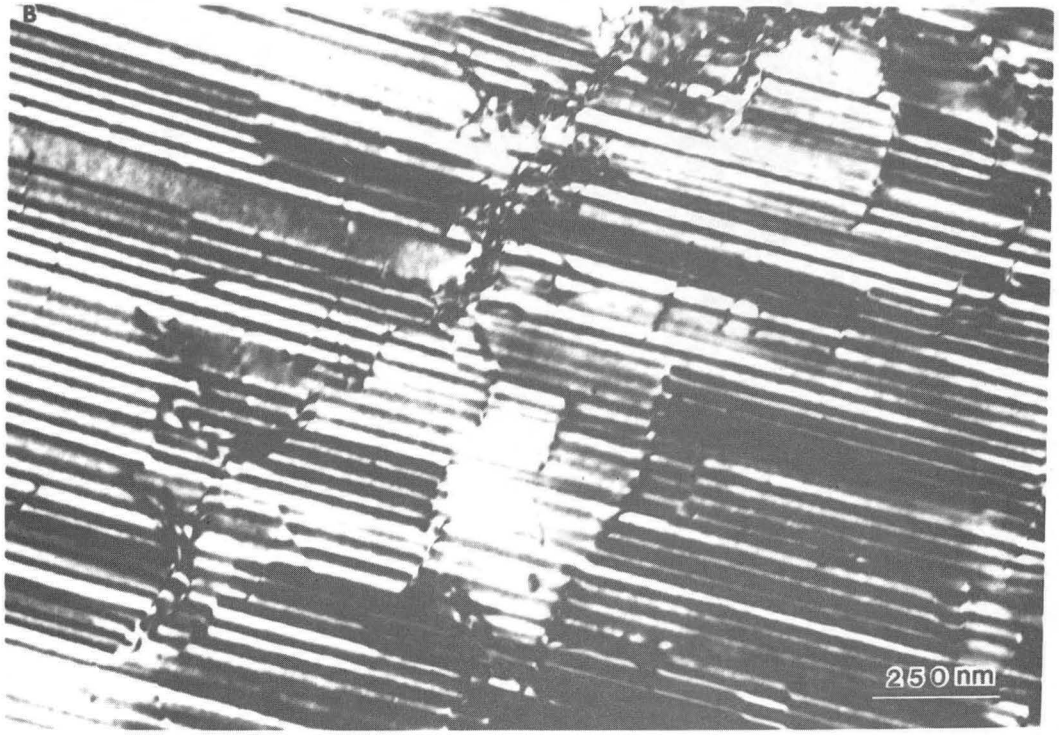

Fig. 24 XBB 876-5097

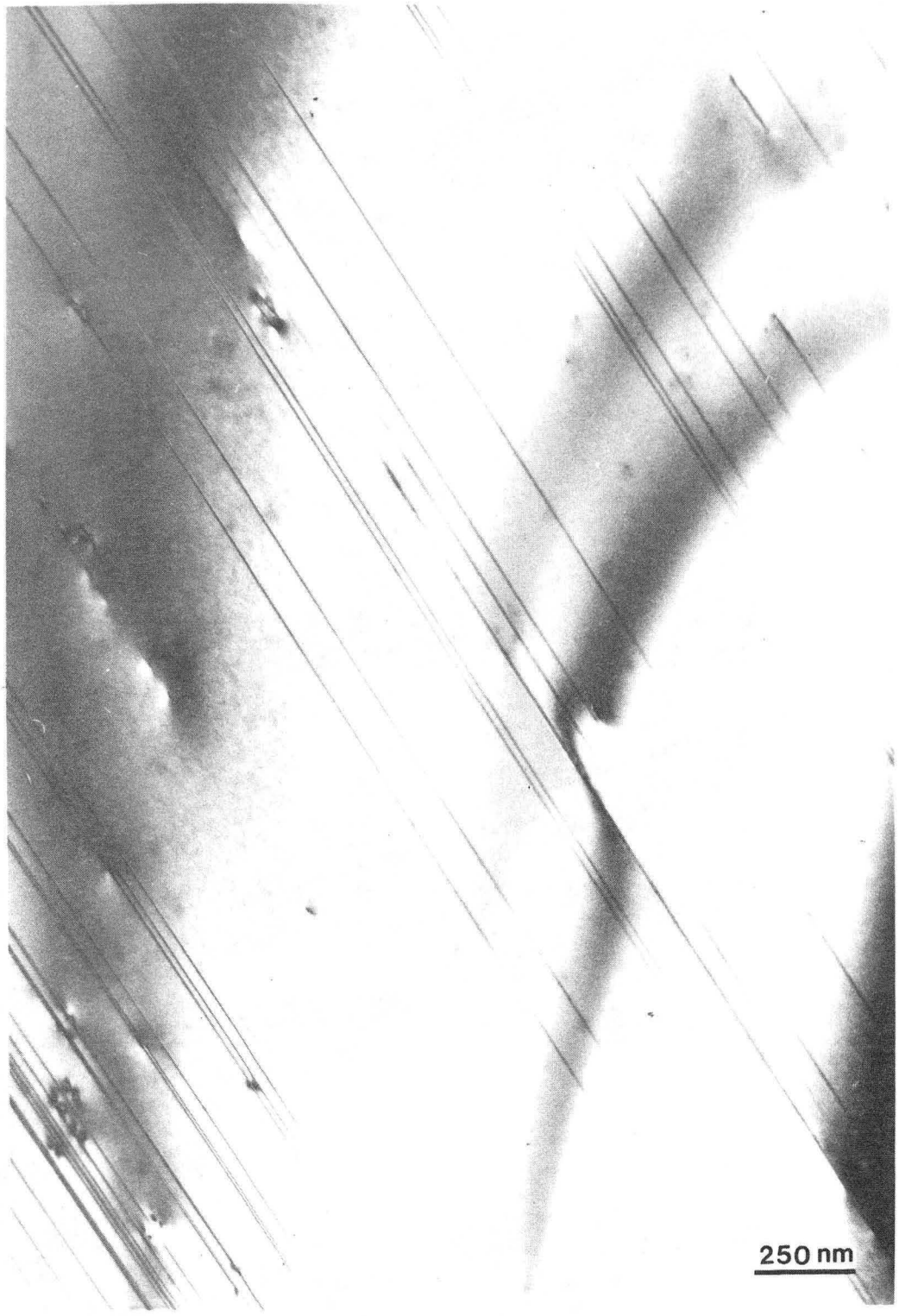

Fig. 25

XBB 876-5098

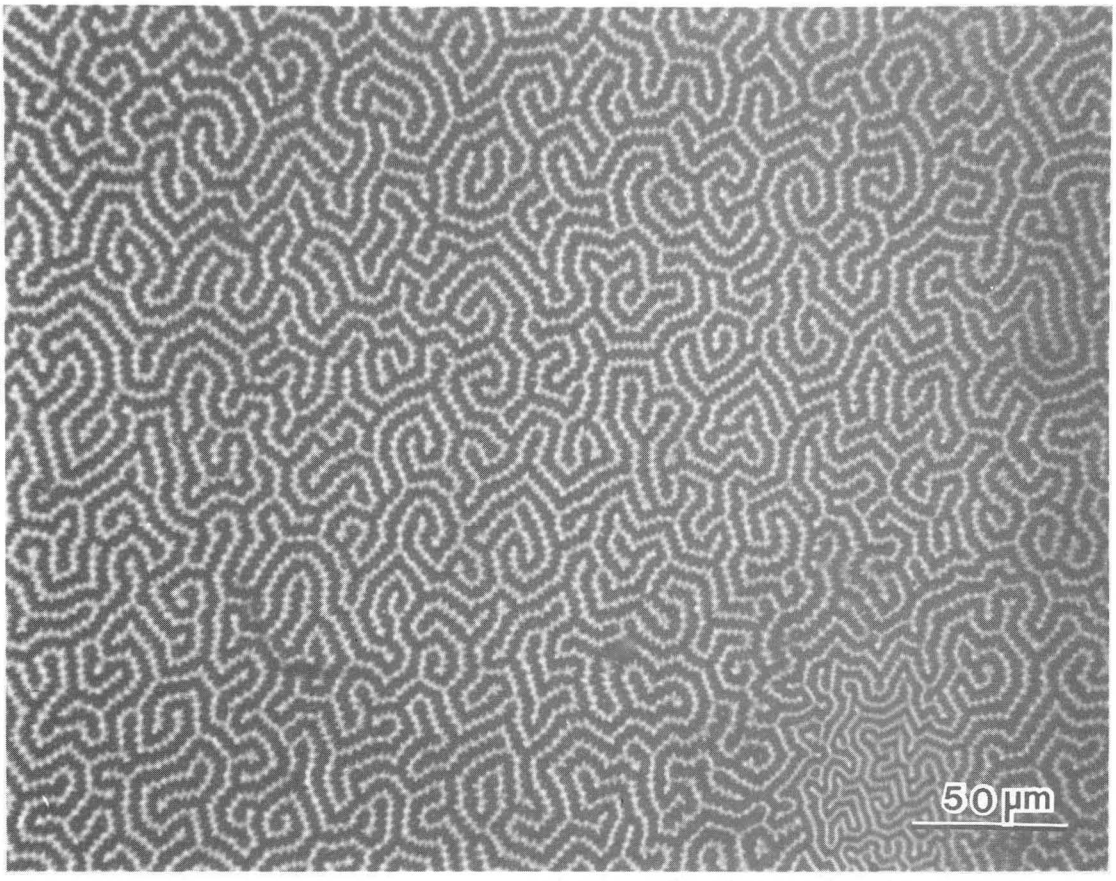

XBB 873-2151

Fig. 26

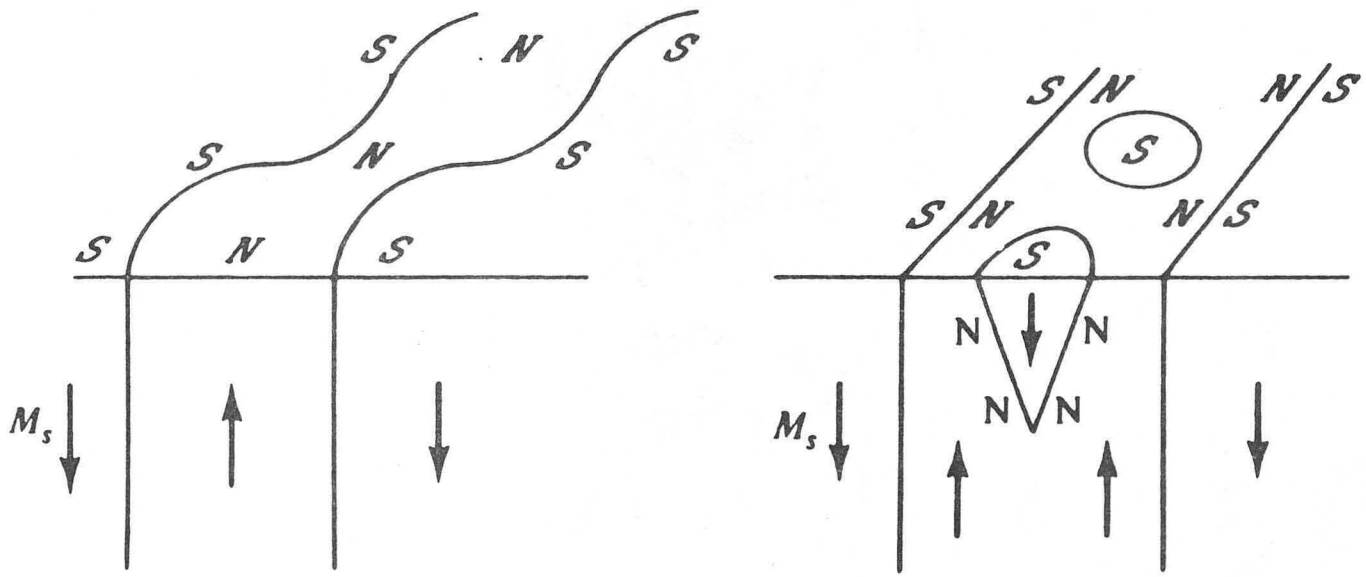

XBL 876-2996

Fig. 27

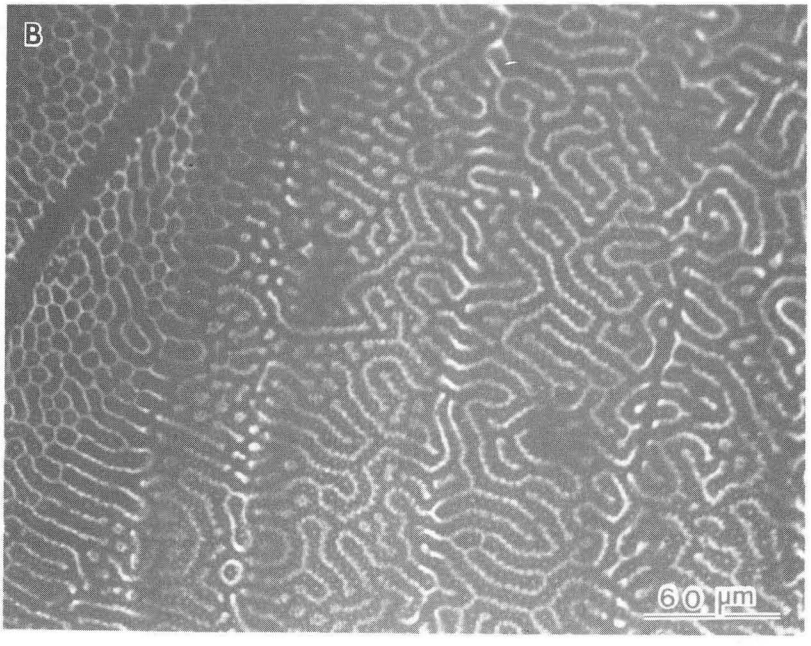

Fig. 28

XBB 860-8647

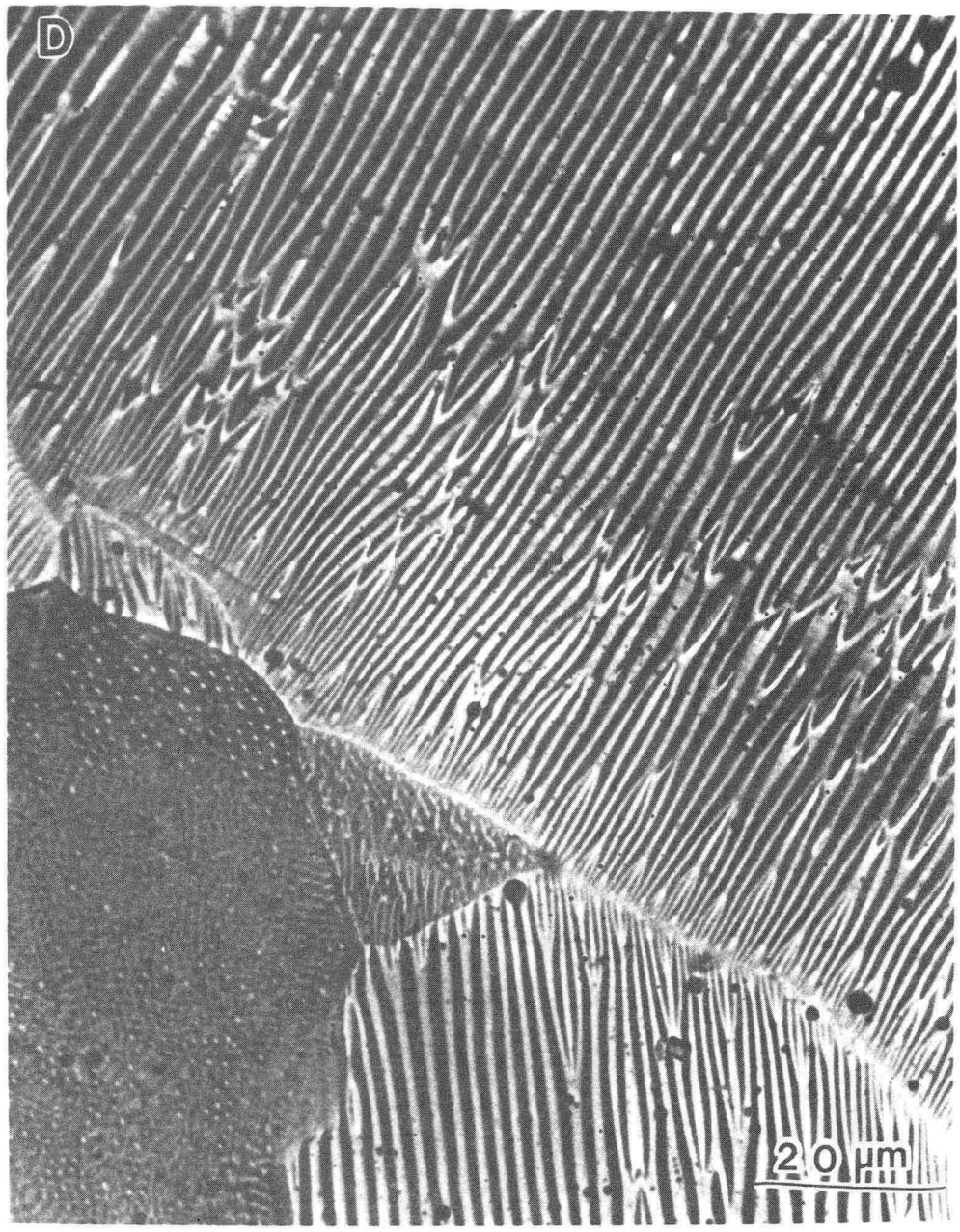

XBB 860-8646A

Fig. 29

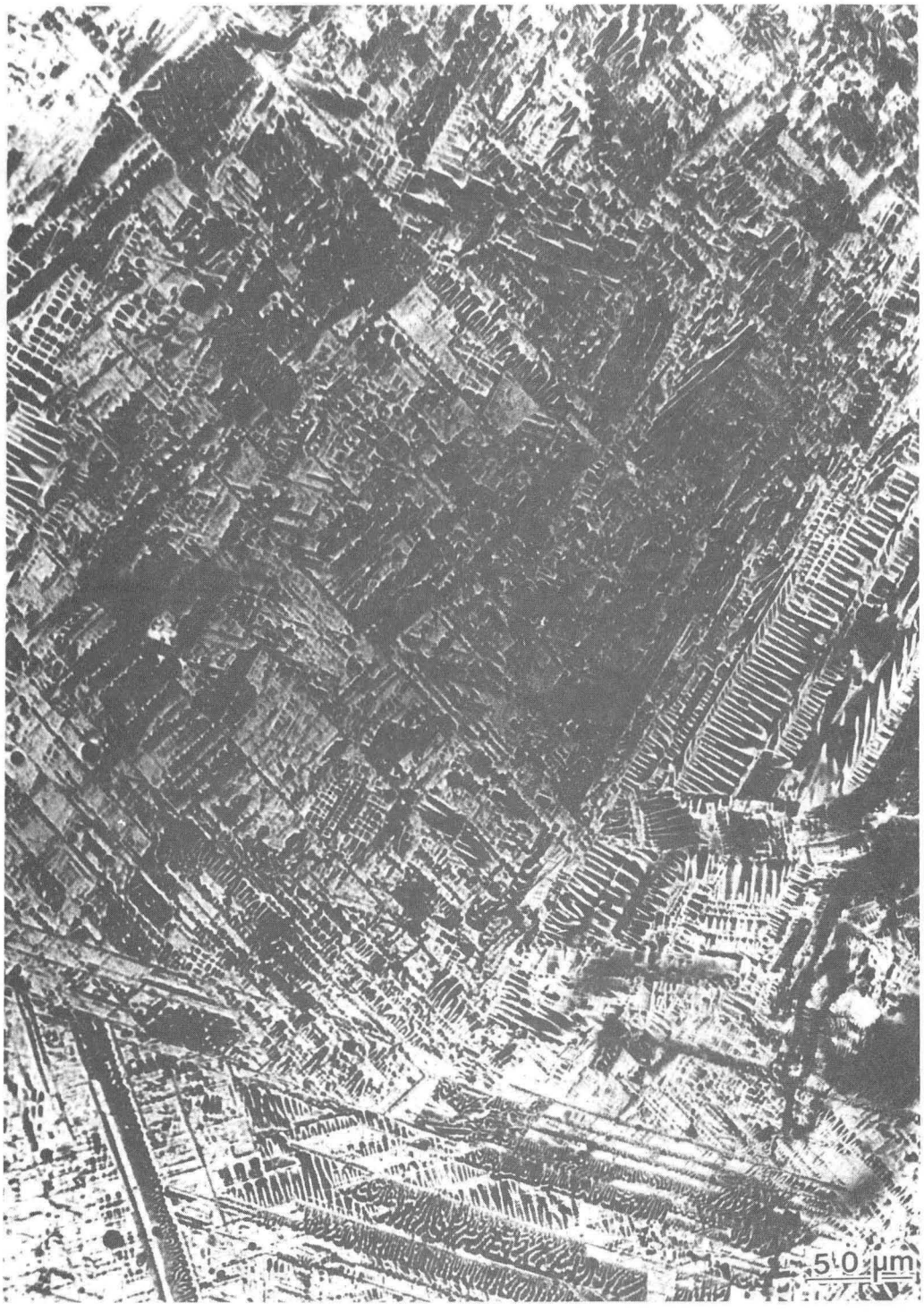

Fig. 30

XBB 860-8649

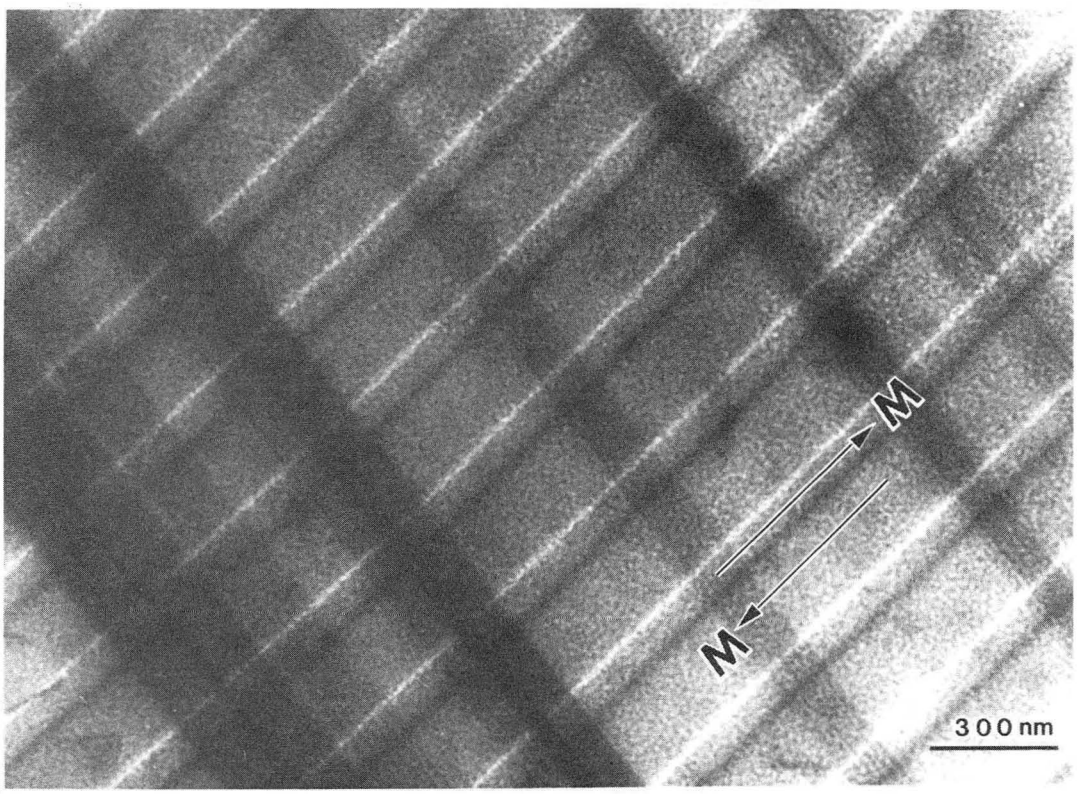

XBB 876-5094

Fig. 31

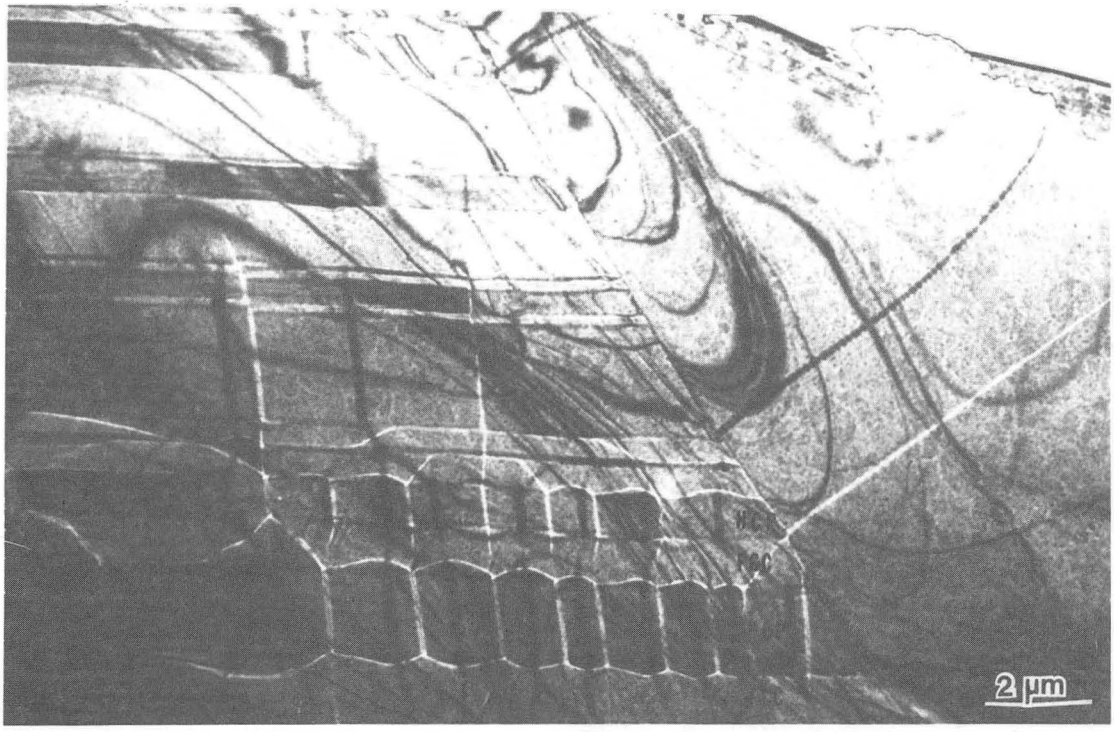

XBB 877-6400

Fig. 32

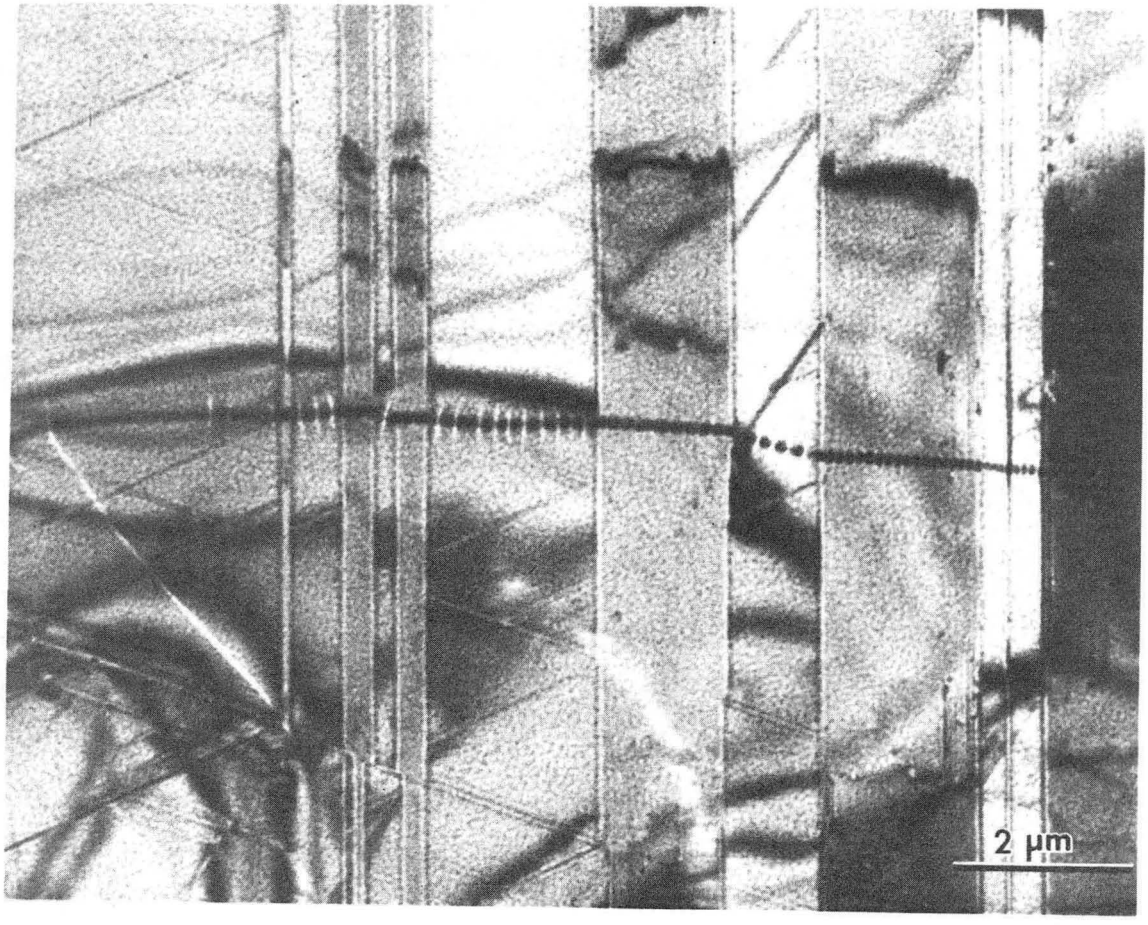

XBB 877-5643

Fig. 33

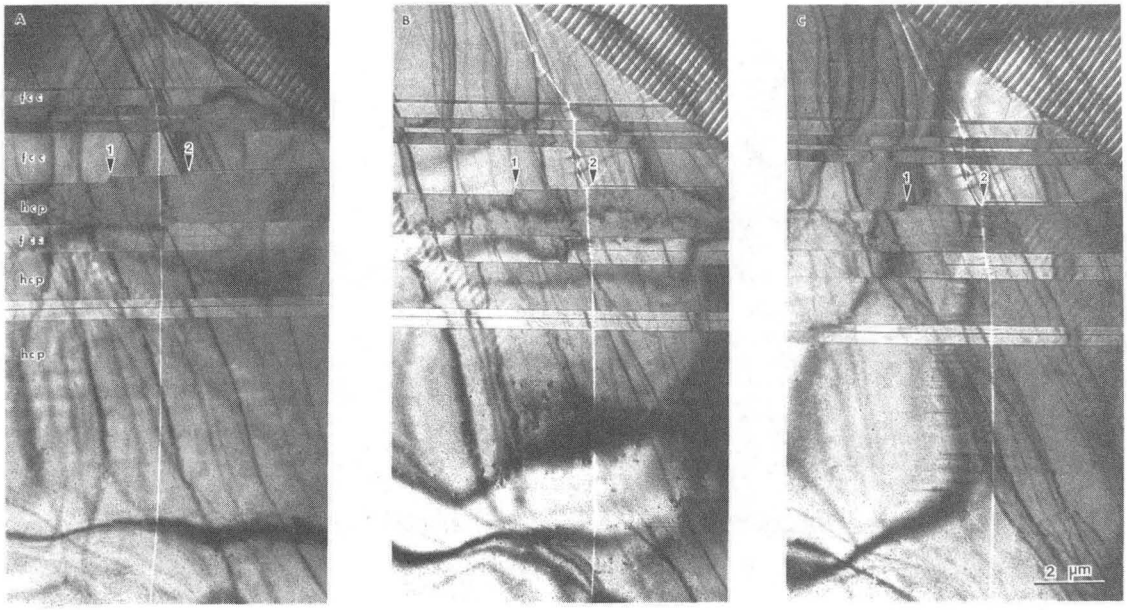

XBB 877-5644

Fig. 34

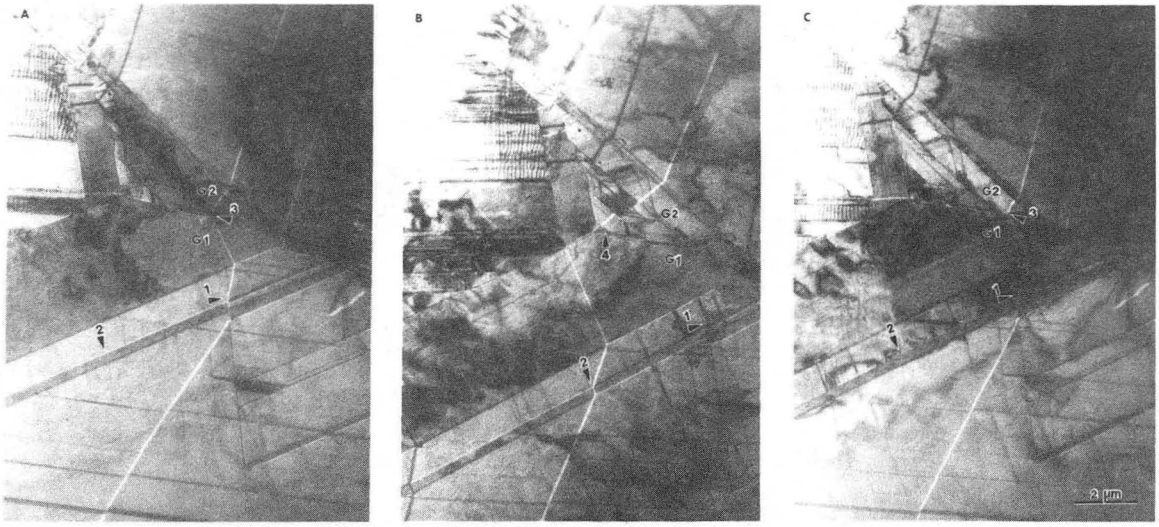

XBB 877 5645

Fig. 35

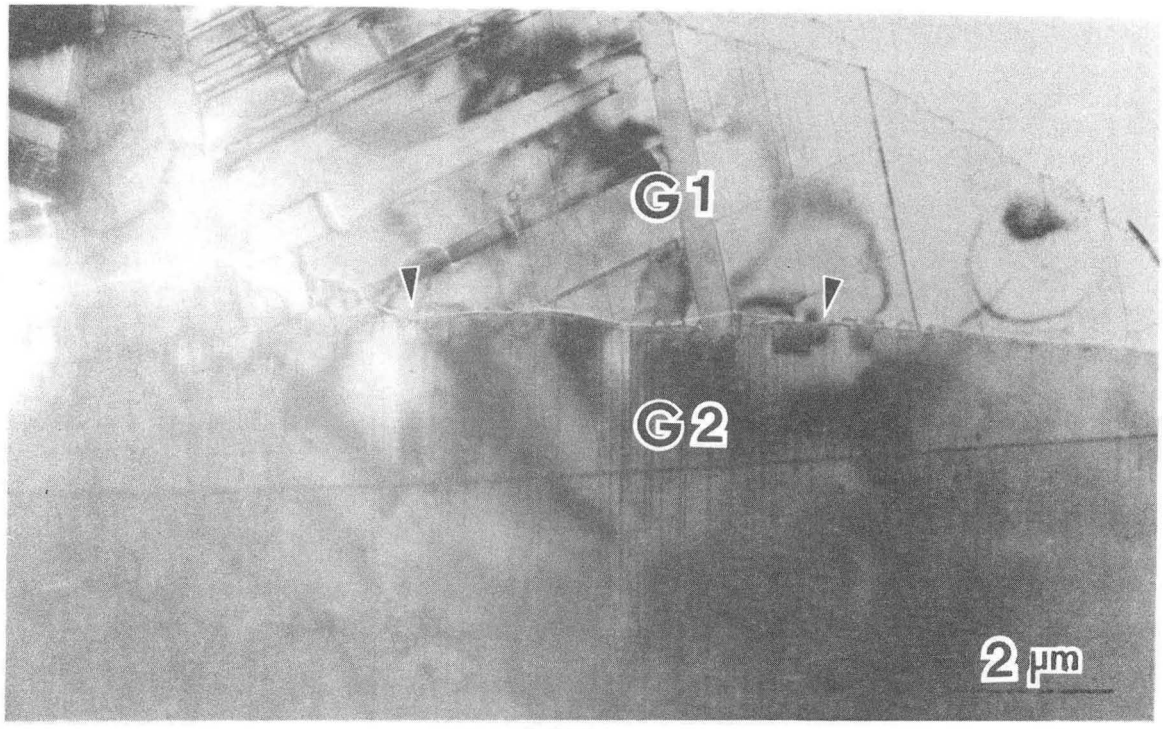

XBB 877-6396

Fig. 36

LAWRENCE BERKELEY LABORATORY
TECHNICAL INFORMATION DEPARTMENT
UNIVERSITY OF CALIFORNIA
BERKELEY, CALIFORNIA 94720